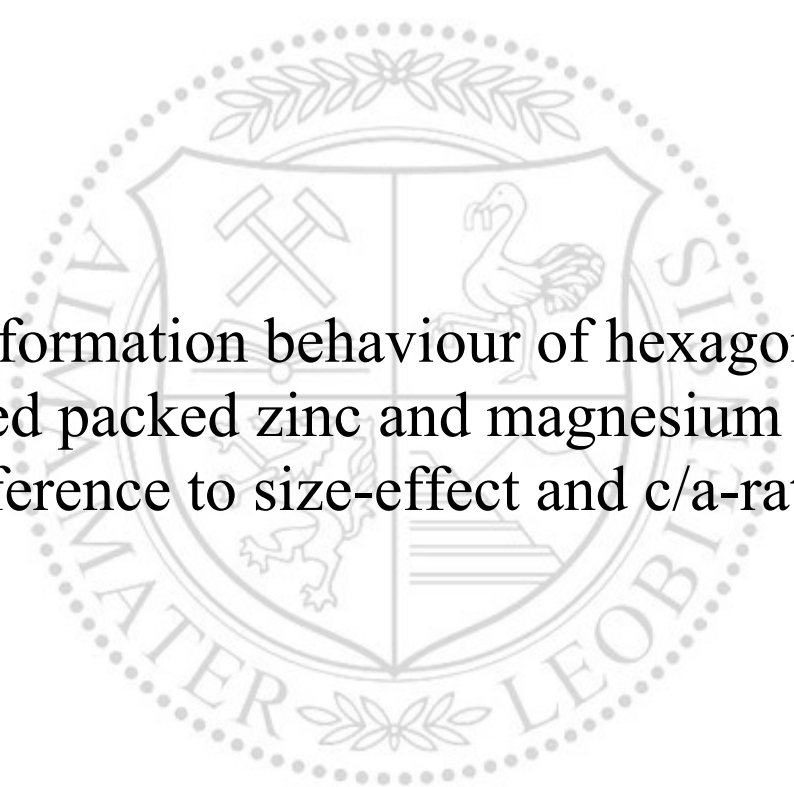Chair of Materials Physics
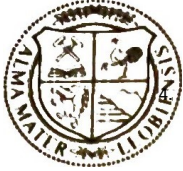
Master's Thesis

Deformation behaviour of hexagonal closed packed zinc and magnesium with reference to size-effect and c/a-ratio

Nadine Susanne Buchebner, BSc

May 2022

MONTANUNIVERSITÅT LEOBEN

mwc.unileoben .ac.at

EIDESSTATTLICHE ERKLÄRUNG

Ich erkläre an Eides statt, dass ich diese Arbeit selbständig verfasst, andere als die angegebenen Quellen und Hilfsmittel nicht benutzt, und mich auch sonst keiner unerlaubten Hilfsmittel bedient habe.

Ich erkläre, dass ich die Richtlinien des Senats der Montanuniversität Leoben zu "Gute wissenschaftliche Praxis" gelesen, verstanden und befolgt habe.

Weiters erkläre ich, dass die elektronische und gedruckte Version der eingereichten wissenschaftlichen Abschlussarbeit formal und inhaltlich identisch sind.

Datum 27.05.2022 .

_____

Unterschrift Verfasser/in

Nadine Susanne Buchebner

Danksagung

Ich möchte hiermit all jenen danken, die mich während meines Studiums begleitet und unterstützt haben, und bei der Anfertigung dieser Masterarbeit unterstützt haben. Insbesondere meinen Betreuern Dipl. Ing. Dr. Markus Alfreider und Assoc. Prof. Dr. Daniel Kiener, welche mir bei jeglichen Fragen und Probleme immer weitergeholfen haben.

Weiters möchte ich mich bei meinem Partner Alexander bedanken, der mir immer zur Seite steht und mir durch jede Krise hilft und jede meiner Entscheidungen unterstützt. Ein besonderer Dank gilt auch meinen Eltern, nur durch deren Unterstützung konnte ich meinen Weg gehen. Dabei möchte ich besonders meine Mutter Helga erwähnen, welche mich nicht nur finanziell unterstützt hat, sondern auch nie müde wurde mich zu motivieren und immer an mich geglaubt hat. Meinen Vater Günter möchte ich dafür danken, dass ich mich immer auf ihn verlassen kann. Auch meinem Bruder Dominic möchte ich dafür danken, dass er mich mit viel Verständnis und Humor durch die Studienzeit begleitet hat. Ein weiterer Dank gilt meiner Freundin Lena, auf die ich mich seit 12 Jahren immer verlassen kann.

Ich danke all meinen Freunden und Kollegen, die meine Studienzeit begleitet und verschönert haben.

Zusammenfassung

In der vorliegenden Arbeit werden mikromechanische *in situ* Zugprüfungen an hexagonal-dichtest gepacktem Zink und Magnesium durchgeführt. Es ist wichtig diese Materialien und ihre speziellen mechanischen Eigenschaften besser zu verstehen, da sie anwendungsrelevant sind, beispielweise für wieder aufladbare Zink-Batterien und biomedizinischen Magnesiumlegierungen, sich aber anders verhalten als kubisch kristallisierte Metalle. In kubischen Materialien haben alle Achsen die gleiche Länge, wohingegen in hexagonalen Kristallen $a = b \neq c$ gilt, wobei das c/a- Verhältnis bestimmend für den Verformungsmechanismus ist. Durch die geringe Anzahl an aktivierbaren Gleitsystemen kann es nämlich zur Bildung von Zwillingen im Material kommen. Ein anderer wichtiger Faktor ist die Größe der Proben, da im Mikrometerbereich ein mechanischer Größeneffekt auftreten kann, welcher wiederum potentiell das Verformungsverhalten beeinflussen könnte. Für die Experimente wurden hochreine (99,999%) Einkristalle verwendet. Diese wurden im fokussierten Ionenstrahl-Mikroskop (Focused-Ion-Beam, FIB) bearbeitet, um besagte miniaturisierte Zugproben mit drei unterschiedlichen Probendimensionen im Bereich von $2\,\mu m$ bis $6\,\mu m$ herzustellen. An diesen wurde in einem Rasterelektronenmikroskop (REM) die Zugprüfung in-situ durchgeführt. Dabei wurden die Proben derart orientiert, dass sie entlang der c-Achse, also in [0001]-Richtung, verlängert wurden. Während des Experiments wurden die Kraft und Verschiebung gemessen, woraus danach Spannungs-Dehnungs-Kurven berechnet wurden, sowie kontinuierliche Videos der Probenverformung aufgezeichnet. Im Anschluss wurden die mechanischen und visuellen Ergebnisse ausgewertet und hinsichtlich der vorliegenden Verformungsmechanismen diskutiert. Der Größeneffekt konnte bei beiden Materialien nachgewiesen werden, und auch verschieden Deformationsmechanismen wie zum Beispiel Zwillinge in Zink und Gleitstufen in Magnesium konnten bestimmt werden.

Abstract

In the present work, in-situ micromechanical tensile tests were carried out for hexagonal close-packed zinc and magnesium. Due to their technological relevance, e.g. for rechargeable zinc-based batteries and biomedical magnesium alloys, it is important to better understand these materials and their specific mechanical properties, since they behave different from cubically crystallized metals. In cubic crystals all axes are of equal length, whereas in hexagonal crystals $a = b \neq c$ applies. This lower symmetry leads to an anisotropy of the mechanical properties, whereby the c/a-ratio is decisive for the deformation mechanism. The limited number of slip systems that can be activated in hcp materials can support the occurrence of twinning. Another important factor is the sample dimension, as a mechanical size-effect can occur in the micron regime, which in turn influences the deformation behaviour. High purity (99.999%) single crystals were used for the experiment. These were processed in the focused ion beam (FIB) microscope to produce micro-tensile specimens, with three dimensions spanning from $2\ \mu m$ to $6\ \mu m$. Subsequently, tensile testing was carried out *in situ* in a scanning electron microscope (SEM). The samples were thereby loaded in such a way that they were extended along the c-axis, i.e. in the [0001] direction. During the experiment, the force and displacement were measured, from which the stress-strain curves were calculated. Furthermore, continuous videos of the specimen deformation were recorded. Afterwards, the results were evaluated and discussed. The size effect could be proven in both materials and also different deformation mechanisms such as twins in zinc and slip steps in magnesium could be determined.

Content

Introduction

1. Introduction

Due to the ever-increasing demands in technology, it is becoming more and more important to research the basic mechanisms of deformation in the various crystal structures. Only by understanding these basic mechanisms it is possible to fully understand the behaviour and influence of alloying elements. As environmental awareness becomes more of a focus, lighter metals are increasingly used, for example to save fuel by reducing weight. Two of these metals of increasing interest are zinc and magnesium, which both crystallize hexagonally.

In order to be able to research these basic mechanisms, it is advantageous to work with highly pure single-crystal materials, as these show good reproducible behaviour due to fewer crystal defects, such as grain boundarys and percipipitations, which in turn would influence the dislocation movements and thus give less information about the mechanisms in the crystal. A special characteristic of hexagonal metals is their different behaviour at different $^c/_a -$ ratios, thus results from one material cannot simply be transferred to another. In fact, this ratio determines the ductility of materials as well as which deformation mechanisms occur and how. Another important topic is the mechanical size effect, which is found in both hexagonal and differently crystallised materials such as fac centred cubic and body centred cubic. Part of this research is to understand how size affects the behaviour of the dislocations and what mechanism prevails as a result. For this purpose, it is beneficial to perform *in situ* micromechanical tests to obtain the strength values and plastic behaviour in relation to the size of the samples [1]–[4].

2. Theoretical principles

The materials used, Zn and Mg crystallize hexagonally and behave differently during deformation than cubically crystallized metals

In the following literature review, the hexagonal crystal structure and the different influences and mechanisms of deformation are discussed, in particular the peculiarities of the hexagonal crystal structure and the deformation behaviour of single crystals. Furthermore, the size effect and its influence on the deformation behaviour is adressed.

2.1. The hexagonal crystal structure

The hexagonal crystal structure is made up of layers of hexagonally arranged lattice points, while the c-axis is not the same length as the a-axis. There are two atoms in each unit cell. To make the symmetry more visible, three unit cells are arranged to form a structural unit [5].
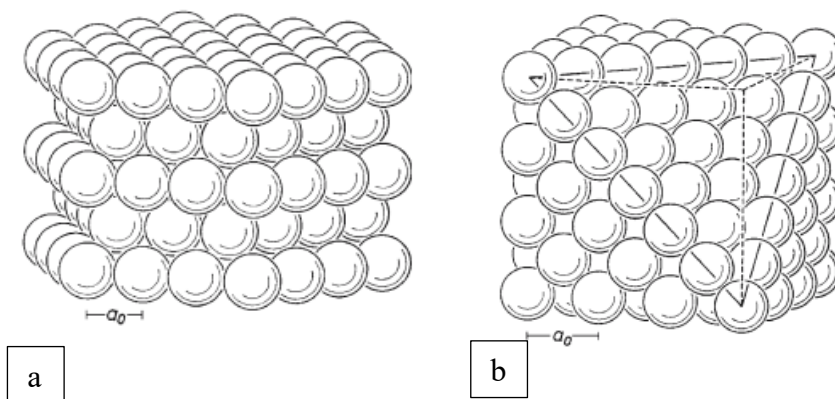

Figure 1: (a) Stacking order of a hcp-crystal, (b) stacking order of fcc-crystal, adapted from [5]

There are two closest packed crystal structures, the hcp and the face-centered cubic (fcc) one. These two structures are closely related, with the single difference that the stacking order is *ABCABC* for fcc and *ABABAB* for hcp, both stacking orders can be seen in Figure 1. Because of the same packing of the fcc and hcp lattice the volume filling and the size of the lattice gaps in the fcc and hcp lattice are equal. The closest packed crystal structures are as tightly packed as possible. Each atom has 12 neighbours of the same kind at the same distance, so the coordination number is 12 [5], [6].

The hexagonal crystal structure

In the ideal hcp structure, the atoms touch in the hexagonal base plane and in adjacent layers, and the $^c/_a$ −ratio is defined as:

$$\frac{c}{a} = \sqrt{\frac{8}{3}} = 1.63$$

Equation 1: Ideal c/a-ratio in the hcp structure

This ratio is approximately correct for pure Mg and Co, but differs for other hexagonally packed metals. Table 1 lists $^c/_a$ − ratios of the most common elements:

	Cd	Zn	Mg	Co	Zr	Ti	Be
$^c/_a$	1.88	1.86	1.62	1.62	1.59	1.58	1.57

Table 1 c/a-ratios of different elements, adapted from [5]

The $^c/_a$ − ratio has a significant influence on the deformation behaviour, which will be discussed in more detail in the following chapters [7][8].

2.2. Deformation in single crystals

Deformation can generally be divided into two types, elastic and plastic, for both single and polycrystalline materials. The main difference is that elastic deformation is reversible and plastic deformation is irreversible when the load is removed [5].
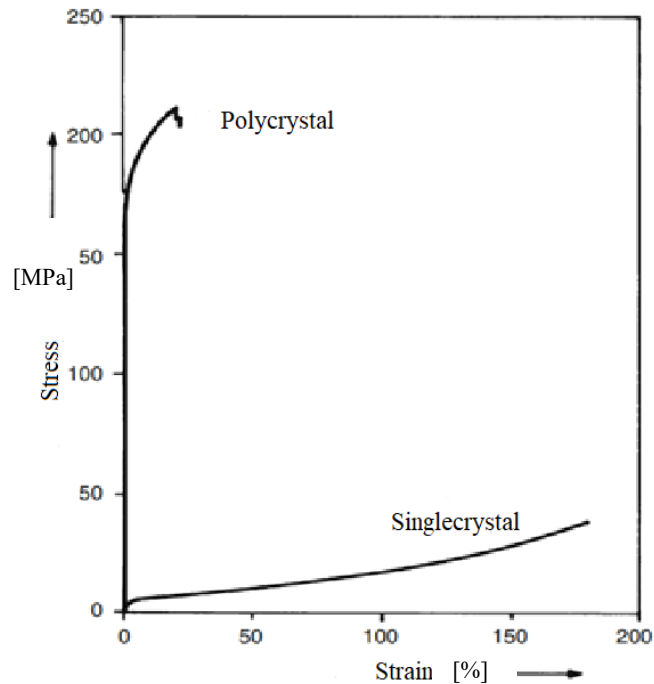

Figure 2: Stress-strain diagram of pure Zn, upper curve polycrystalline, lower curve singlecrystalline, adapted from [5]

The difference in the deformation behaviour of polycrystals and single crystals lies in the different orientation of the individual crystal grains in the polycrystal. The different deformation behaviour can be seen in Figure 2 [5], with the single crystalline (sc) material withstanding higher strains and the polycrystalline (pc) withstanding more stress, but hardly any strain. Due to the fact that not all grains deform at the same time in pc materials, a higher ductility can be observed in sc materials than in pc materials [9].

The elementary mechanism of plastic deformation is that a certain stress can move the dislocations, causing atoms to move one after the other in time. A dislocation can be defined as a disturbance along lines in the perfect crystal structure [5]. Plastic deformation of sc materials can be distinguished between two major types: Sliding and twinning. Dislocations are already present in the crystal interior before the onset of deformation, and the dislocations belong to crystallographically defined slip systems.
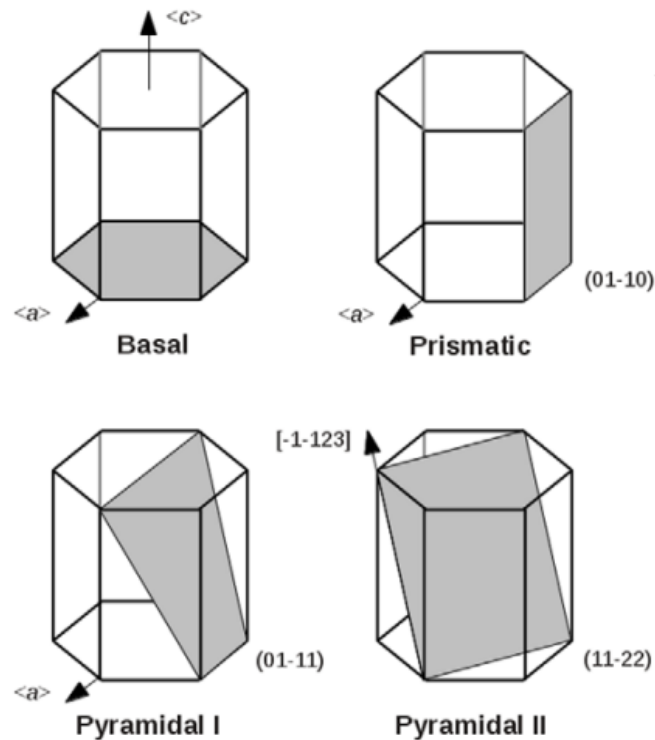

Figure 3: Slip systems in hcp crystals, adapted from [13]

In order for plasticity to begin, the dislocations slide through the material resulting in crystal planes sliding along each other [9]. A slip plane with a slip direction represents a slip system. There are preferred slip directions and planes as well as a certain number of slip systems in the different crystal structures [5], [9], [10].

In hcp crystals there are four common slip systems, basal $< a >$, prismatic $< a >$ and second order pyramidal $< c + a >$.

The most densely packed planes are preferred as sliding planes because they provide the least frictional resistance against the movement of the dislocations. Figure 3 [13] shows the different slip systems in hcp crystals.

The densest packed planes and directions for the hcp crystals are the (0001) $-$planes and the $< 11\bar{2}0 >$ $-$directions, whereby only two of these resulting sets are independent slip systems, as the deformation of one of the three slip systems can also be achieved by combining the deformation of the other two systems.

The sliding, as mentioned before, takes place on preferred planes and directions, and is caused by dislocation movement. For the dislocations to move, a certain amount of stress must be applied, otherwise the resistance against the dislocation movement will not be exceeded. Sliding can therefore only occur when the shear stress in the sliding direction on the sliding plane exceeds a critical value, which is known as critical resolved shear stress (CRSS and can be described by Schmid`s Law:

$$\tau_c = \sigma \cos \Phi \cos \lambda$$

Equation 2: Schmid`s Law, adapted from [9]

In this case τ_c is the CRSS, σ is the tensile stress, φ is defined as the angle between the direction of the applied force and the slip direction and λ is the angle between the normal of the slip plane and the direction of the applied force. The so called Schmid's orientation factor m (m $= \cos\phi\cos\lambda, 0 \leq m \leq 0.5$) provides information on how the orientation of the crystal affects the tolerable stress [9]. In addition, the Schmid factor is used to predict the type of sliding system that could be activated [7]. The orientation is called soft when $\lambda = \phi = 45°$ and $\tau = \sigma/2$, here dislocation movement is activated at the lowest tensile stress. A hard orientation results when $\lambda = 90°$ or $\phi = 90°$ and therefore $\tau_c = 0$. This shows that the crystal orientation strongly affects different dislocation motion under the same conditions and influences the deformation. If there are many slip systems in a crystal, more spatial orientations can be assumed during the slip. Hcp crystals have only three slip systems, in comparison body-centered-cubic (bcc) crystals posses *48* and cubic face-centered crystals *12* slip systems [9]. The number of slip systems does influence the plasticity of crystals, but it is not universally valid, as it also depends on whether the slip systems can be activated simultaneously.

This is the case for fcc-crystals, but not necessarily bcc-crystals. Therefore fcc-crystals have a better plasticity despite having less slip systems since the systems activate simultaneously [9], [10].
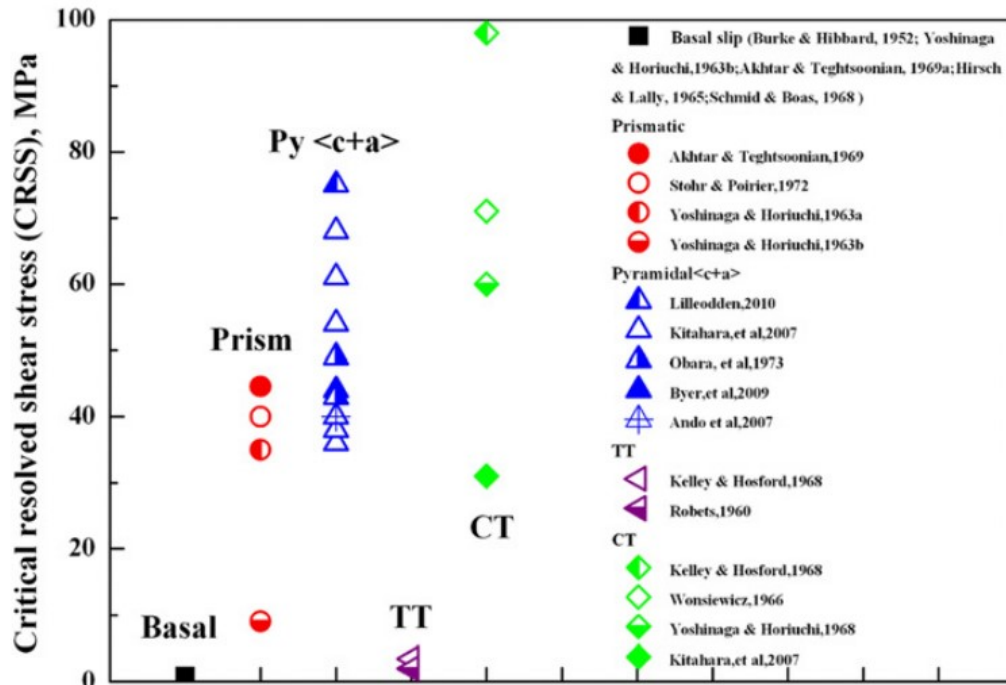

Figure 4: CRSS for different Deformation Mechanisms, TT= tension twin, CT= compression twin, adapted from [11]

Figure 4 [11] lists the CRSS values for various deformation mechanism of Mg at room temperature. The experimentally obtainable CRSS is influenced by temperature, impurities, dislocation density, deformation mechanism, strain rate etc. The influence of these factors must be considered individually for each material [12][9].

When the crystal is prevented from sliding, deformation twinning can occur as an alternate plasticity mechanism. Therefore, due to the applied shear stress some parallel crystal planes in one part of the crystal produce a uniform shear with a certain distance and direction to each other.
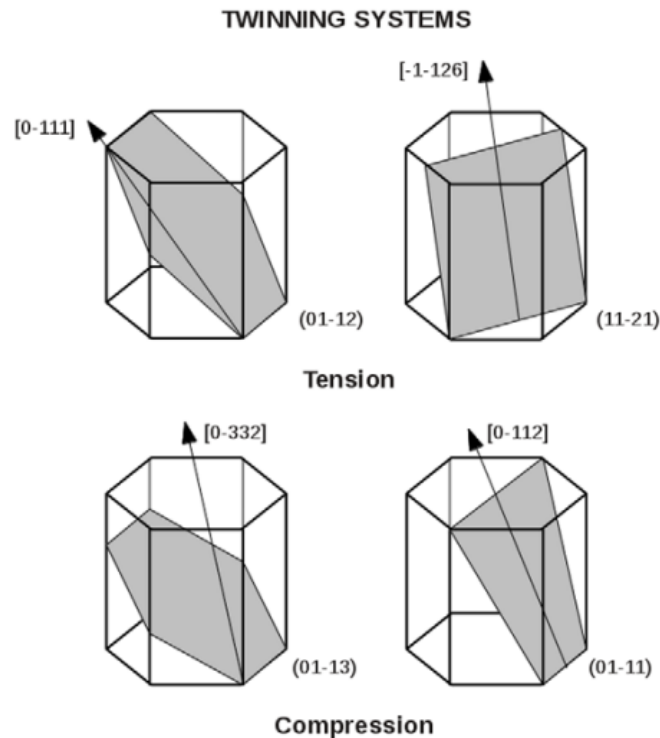
TWINNING SYSTEMS

Figure 5: Different twinning systems of hcp crystals, adapted from [13]

In this way, a twinned crystal is formed, which consists of a deformed and an undeformed part. The boundary between these parts is called twin boundary and the direction of motion of the twin plane becomes the twin direction. In bcc and hcp crystals, it is common for the relative displacement of each layer of the crystal plane parallel to the twinning plane to be constant in the shear zone. Twin deformation also occurs under the action of shear stress, usually in the stress concentration zone due to sliding resistance. Due to this circumstance, the CRSS for twinning is much higher than that for sliding. Twinning is uniform shear over a larger volume compared to sliding, where sliding directly leads to plastic deformation and twinning forms a new crystal orientation that leads to new slip systems and therefore indirectly affects dislocation plasticity [9]. Figure 5 [13] shows the four different twinning systems, divided in compression and tension, in hcp crystals.

Another difference to sliding is the monosingularity of the twin system, i.e., the shearing movement for twinning can only take place in one direction and not in the reverse direction. This results in limitations in the activation of twin systems. For cubic crystals, it is always the case that at least one of the 12 twin systems supports the imposed change in shape, such as elongation in the direction of tension during tensile deformation. This is not the case if the three principal axes of the lattice are not equivalent, as in hexagonal crystals, as can be seen in Figure 6 [4].
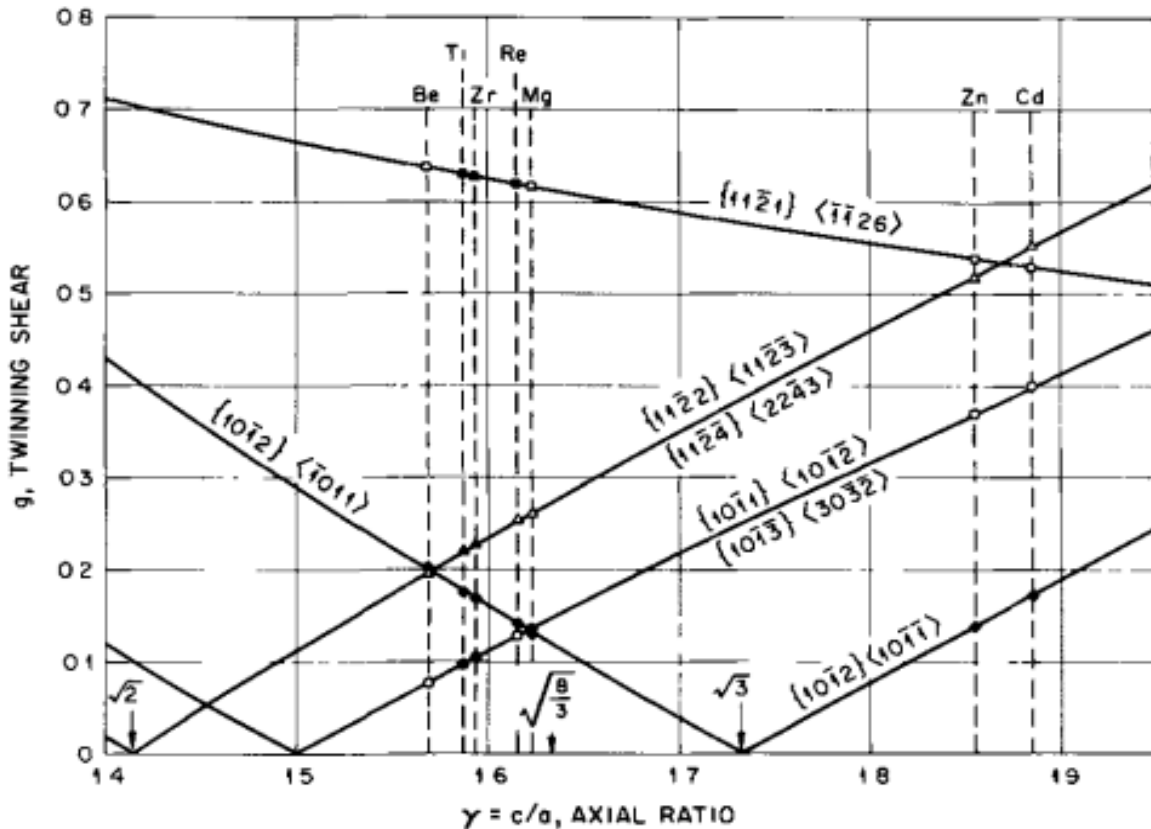

Figure 6: c/a-ratio of hexagonal materials, the filled symbol marks the active twinning mode [4]

Depending on the c/a ratio, the crystal is shortened or lengthened in comparison of the hcp lattice perpendicular to the base plane. The c/a ratio also influences which twin system occurs during deformation. For example, the $\{10\bar{1}2\}$ twin occurs as a compression twin for Cd and Zn ($c/a > 1.73$), since the shear direction for the $\{10\bar{1}2\}$ twin reverses at 1.73 ($= \sqrt{3}$). The $\{10\bar{1}2\}$ twin is a tensile twin for all other hcp metals with respect to the c-axis [4].

For Zr and Ti, more than one twin system is active for either twin type at low temperatures. As we can see in Figure 6 [4], the $\{11\bar{2}1\}$ twins form additionally to the $\{10\bar{1}2\}$ tension twins and $\{11\bar{2}2\}$ twins additionally to the $\{10\bar{1}1\}$ compression twin.

Deformation in single crystals

Due to the included $\{11\bar{2}1\}$ twins, higher ductility can be observed for Zr and Ti in particular, after pre-stressing [4].

Hexagonal metals with high ductility (e.g. Re, Zr, Ti) are able to twin in compression and tension, whereas metals with limited ductility (e.g. Zn, Be) deform only with the $\{10\bar{1}2\}$ twin. Twinning has a good influence on plastic flow by rearranging unfavourably oriented grains into a more favourable position by twinning and sliding. The plastic flow can be significantly improved by the occurrence of second order twins, for example $\{11\bar{2}1\}$ twin in $\{10\bar{1}2\}$ twin in Zr or a $\{1011\}$ twin in $\{10\bar{1}2\}$ Mg. Third order twinning and even higher can be observed in Zr and its alloys. Within materials such as Zr and Ti where second-order twinning takes place, mutual intersections of twins occur and dislocations are incorporated into twins. Twinning can have a positive effect on plastic deformation. In more brittle materials such as Zn and Be, which have only one twin system, the occurrence of a twin leads to a local stress concentration and can result in crack nucleation [4].

A different influence of the c/a ratio can be observed for the Schmid factor. Nan *et al.* [7] [8] provide the calculation of Schmid factors for different hcp metals and their correlation with the c/a-ratio:

$$cos\phi cos\lambda = m = \frac{[u_1 u_2 + v_1 v_2 - \frac{1}{2}(u_1 v_2 + u_2 v_1) + (\frac{c}{a})^2 w_1 w_2]}{[(u_1^2 + v_1^2 - u_1 v_1 + (\frac{c}{a})^2 w_1^2)(u_2^2 + v_2^2 - u_2 v_2 + (\frac{c}{a})^2 w_2^2)]^2}$$

Equation 3: Calculation of Schmid factor, adapted from [4]

$[u_1\ v_1\ w_1]$ are the indexes of the slip (twinning) plane normal or slip (twinning) direction and $[u_2\ v_2\ w_2]$ the indexes of the loading direction. Due to the influence of the c/a ratio on the Schmid factor, there is again an influence on the CRSS. [8].

2.3.Size effect

A mechanical size effect describes the influence of sample size on the deformation behaviour and physical properties of a material. An example is the increase in the yield strength of metal alloys through grain refinement, whereas the yield strength is proportional to the inverse square root of the grain size. This behaviour is described by the Hall-Petch equation and is based on accumulation of dislocations at grain boundaries. However, this effect fails if the grain size is too small, since a dislocation ring must fit into a grain [14].

Parthasarathy *et al.* [15] provided a simplified explanation of this similar effect in micro-to-nanoscale geometries, given the stochasticity of dislocation source lengths in finite sized samples. Although the geometric factor is uncertain, the stress to activate a source whose one end is pinned and the other is at the free surface of the cylinder is proportional to that of a Frank-Read source [15]. The CRSS of a cylindrical specimen R with height h and orientation of the primary slip plane at angle beta to the loading axis can be defined as:

$$CRSS = \frac{\alpha Gb}{\overline{\lambda}_{max}} + \tau_0 + 0{,}5\, Gb\, \sqrt{\rho_{tot}}$$

Equation 4: Calculation of the CRSS, adapted from [12]

Size effect

Where α is a geometric constant, G is the shear modulus, b is the Burgers vector, τ_0 is the friction resistance, ρ_{tot} is the total density of dislocations and $\bar{\lambda}_{max}$ is the mean value of the source length. For a better understanding, Figure 7a shows how a double-pinned Frank-Read source transforms into two single-ended sources in a finite sample [15].
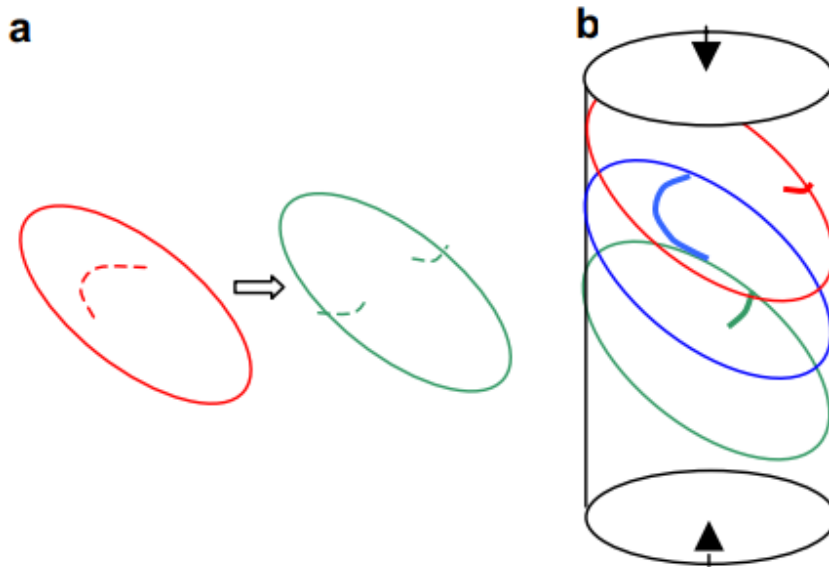

Figure 7: Sketch of how a double-pinned Frank-Read source become single ended sources, adapted from [15]

Figure 7b shows single-ended sources in a finite cylindrical sample in a critical configuration. This occurs where the distance between the pin and the free surface is at the minimum. The blue arm here is the longest among the available sources and is thus determinant for the CRSS. This means that the statistics of the pins within a sample of finite size determines the yield strength [15].

Armstrong *et al.*[16] compares the twin stress with the slip stress as a function of grain size, where the Hall-Petch relationship applies but the slope for twinning is up to 10 times greater than that for ordinary dislocation plasticity. It is not fully understood how this difference arises, but in this study it is explained by the activity of the dislocations that occur before plastic deformation, whereas yield stress is generally related to plastic deformation [16]–[18].

$$\sigma = \sigma_0 + k_T d^{-\alpha}$$

Equation 5: Hall-Petch for twinning,adapted from [16]

Size effect

In the equation above k_T stands for the twinning slope, σ is the flow strength and α $(= 0.5 -$ $1)$ and σ_0 are size independent constants.

It is suggested that microplasticity and in general deformation is determined by various influences, such as elastic anisotropy, incompatibility stresses and the impediment of sliding by barriers. For example, the Hall-Petch slope for twinning in copper (fcc) is $k_T = 0.7\ MN/m^{\frac{3}{2}}$ [17] and for slip $k_S = 0.35\ MN/m^{\frac{3}{2}}$ [17]. In Zr (hcp), an even greater difference can be observed, here the value for twinning is $k_T = 2.4\ MN/m^{\frac{3}{2}}$ [17] and for slip $k_S = 0.25\ MN/m^{\frac{3}{2}}$ [17]. Yu $et\ al.$ [17] present a "stimulated slip" model to explain the size dependence of deformation twinning. Thus, in ordinary dislocation slip, inelastic shear motions should be distributed between slip planes, whereas for deformation twinning there must be perfectly correlated layer-to-layer shear, i.e. the total slip (twinning dislocation) must have the same Burgers vector at atomic neighbouring planes [17],[18].

Microcompression tests and in-situ compression tests with single-crystalline Ti alloys could show that the stress required to form deformation twins increases strongly with decreasing size of the samples [17], [19].

Jeong $et\ al.$ [20] carried out in-situ micro-compression tests on Mg pillars in SEM and transmission electron microscope (TEM). Among other things, the size effect was investigated. It was shown that the pile-up of prismatic $< a >$ dislocations serves as a local stress concentration for twin nucleation. The nucleation of the twin does not occur directly from the pile-up of the prismatic $< a >$ dislocations, but through the cross slip of the prismatic $< a >$ dislocations to the basal plane. A series of successive dislocation-dissociation reactions results in the formation of a twin between the prismatic $< a >$ dislocations and basal stacking faults. Through investigation in the TEM it was shown that not only the dislocation pile-up but also the dissociation reaction of the dislocations with the formation of the stacking faults play a major role. This was shown for pillar sizes between 0.5 and $4\ \mu m$.

Greer $et\ al.$ [21] distinguished between the intrinsic and extrinsic size effect. The intrinsic size effect relates to microstructure, grain and precipitate size, twin boundary spacing and the density of dislocations and affects materials of any dimensionality. The extrinsic size effect refers to the sample size. Their influence on strengthening mechanisms such as work hardening, precipitate hardening and grain boundary strengthening is discussed.

For this work, strain hardening is of particular interest, as it depends on dislocation movement and generation and is therefore observable in sc materials. It is pointed out that the intrinsic size effect emerges for sizes in the micrometre or sub micrometre range. One theory of size dependence for microcompression columns is "dislocation starvation". As the samples are so small, it is more likely that the dislocation will find a free surface and annihilate rather than multiply. Therefore, plasticity here is influenced more by nucleation and movement of newly formed dislocations than by interaction and movement of existing ones. Greer *et al.* [22] showed that by eliminating defects in sub micrometre gold crystals, the strength is up to 50 times higher than in bulk samples. This could in turn be attributed to the absence of dislocations in the crystal. The theoretical stress cannot be achieved because a layer forms on the sample during preparation in the FIB, which introduces dislocation loops into the crystal, which in turn create an obstruction for the dislocations to leave the crystal, thus dislocations remain in the crystal. This mechanism is in contrast to the conventional strengthening mechanism for bulk materials, where defects are introduced into the crystal to increase strength [22].

Another explanation for the behaviour of small samples is provided by Dimiduk *et al*. [23]. The effect of the largest average distance between internal pinning points such as forest dislocations and the free surface on the dislocation movement is considered here. It was observed that samples below $\sim 16 \ \mu m$ show a strong size effect in sc Ni [23]. This results in higher strain hardening with decreasing specimen diameter and thus higher CRSS values for smaller diameters. An option is the dominance of dislocation-dislocation interactions in bulk hardening at larger diameters and source exhaustion at smaller diameters [24].

One other possibility to influence the deformation behaviour and to increase the hardening is the trapping of dislocations in the crystal. Ng *et al.* [25] coated pc aluminium with tungsten and were able to trap the dislocations in the material, resulting in a smoothed stress-strain curve and an increased strain hardening rate (SHR) [25].

2.4. Deformation behaviour of Mg

Due to its high strength-to-weight ratio, Mg and its alloys are of great interest to the transportation industry. As mentioned above, Mg has an hcp structure and deforms mainly via dislocation slip (basal $< a >$, prismatic $< a >$ and pyramidal $< c + a >$) and deformation twinning.

The basal conduction $< a >$ seems similar to the deformation mechanisms in fcc-materials, as the dislocations easily nucleate and slide on this plane, although anisotropic deformation behaviour prevails in hcp-materials.

In contrast, the $< c + a >$ pyramidal slip behaves quite different from the basal one, as the Burgers vector is large and the Peierls stress for pyramidal planes is very high, preventing the dislocations from sliding.

The deformation modes in Mg show large differences in activation energy, as a result a strongly anisotropic behaviour can be observed as a function of loading axes and conditions [1].

The most commonly observed twinning plane is the $\{10\bar{1}2\}$ plane in the $< 10\bar{1}\bar{1} >$ direction, not only for Mg but also for some other hcp metals, as depicted in Figure 6.
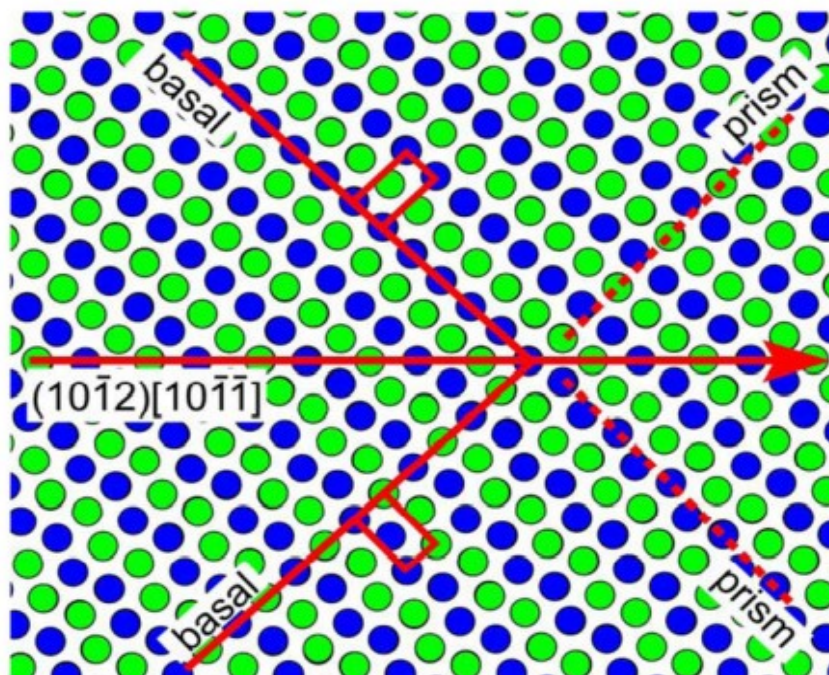
Figure 8: Movement of the atoms at the twin boundary, adapted from [26]

The twin scheme cannot be achieved simply by homogeneous shearing, which is again a difference to fcc-metals. Due to the high symmetry in fcc-systems, twinning and growth can be controlled by defined partial dislocations, the twinning plane being the most densely packed {111} plane. In contrast, no twinning takes place at all on the most densely packed plane {0001} in hcp crystals. It is unclear whether partial dislocations are responsible for the twinning, observed in Mg.

Li *et al.* [26] explained why $\{10\bar{1}2\} < 10\bar{1}\bar{1} >$ twinning mode is found most often. The growth of the deformation twin due to the displacement of the twin boundary is caused by atomic shuffling in the two $\{10\bar{1}2\}$ planes of the parent lattice, which is directly adjacent to the twin boundary. This forms a twin with a 90° misorientation to the matrix, as a reorientation of the lattice where the basal plane becomes the prismatic plane and the other way around, occurs. Furthermore, this process does not require a well-defined dislocation movement. In fact, the dislocation movement on this plane is still matter to ongoing research [26].

Figure 8 [26] shows the magnified view of the twin boundary, with the red arrow marking the direction of the twinning. The red box indicates the repeating basal unit in the matrix, which is perpendicular to the one in the twin. The flat basal plane in the matrix becomes the plane of the corrugated prismatic plane in the twin, while the corrugated prism plane in the matrix becomes the flat basal plane [26].

Wang *et al.* [27] studied the identification of twinning disconnections (TDs). TDs can be described with a Burgers vector b and a step of height h, where the step height can be expressed where qh_0, h_0 $equals$ d_{AA} which is the spacing between compound κ_1 and crystallographic planes and q is an integer. Thus, the TDs are denoted by (b, qh_0). The study examines the TDs of $(\bar{1}011)$ and $(\bar{1}013)$ twins, which, in contrast to $(\bar{1}012)$ twins, accommodate only uniaxial compression along the c-axis for all c/a- ratios. The $(\bar{1}012)$ twin accommodates uniaxial extension along the c-axis and two possible TDs are examined for each twin type.

As found in previous studies, the large asymmetry is also suggested to be the major driving force for the $(\bar{1}011)$ twin and $(\bar{1}013)$ twin being active only under compressive loading on the c-axis, but not under tensile loading.

On the contrary, the $(\bar{1}012)$ twin is active under tensile load. These asymmetries explain which type of twin is dominant in pc deformation.

Another interesting feature is the qualitative equality of the $(\bar{1}011)$ and $(\bar{1}013)$ twin, depicted in Figure 27, despite having quite different twin plane orientations, but the same zone axis. They are both equally different from the $(\bar{1}012)$ twin, where there are no microshuffles required for twinning to take place [27].
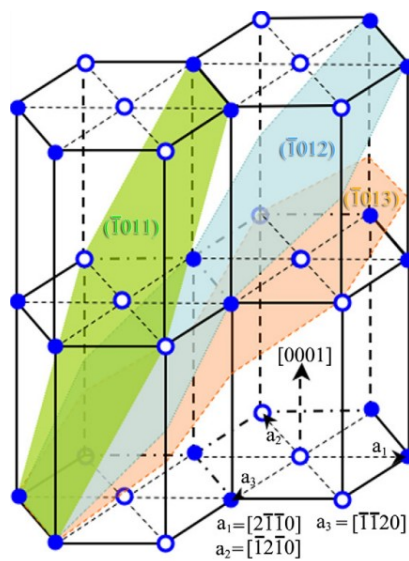

Figure 9: Hcp-lattice with the twinning planes $(\bar{1}011)$ $(\bar{1}013)$ *and* $(\bar{1}012)$ *[27]*

When a TD moves, the atomic displacement can be described as a shear, produced by the Burgers vector b plus a series of shuffles, with shuffle displacement in the dichromatic complex. In the dichromatic complex the atom sites from both crystals are included and corresponds to the interpenetration of both A and B sites.

The solid circles represent Atoms in A-type plane $(\bar{1}2\bar{1}0)$ und the empty circles atoms of the B-type plane $(\bar{1}2\bar{1}0)$. Between the A and B-type $(\bar{1}2\bar{1}0)$ planes the spacing is $a/2$, where a is the lattice constant. For twin families with the same zonal axis, two types can be distinguished, A and B type, which follow the stacking order of the $(\bar{1}2\bar{1}0)$ crystal plane. In the hcp lattice, the two types alternate but do not always have the same spacing.

As a conclusion, this study predicts that the mechanism of motion of $(b, 4h_0)$ TDs is the same for $(\bar{1}011)$ and $(\bar{1}013)$ twins, entailing synchroshear shuffle dislocation motion with vectors that belong to the dichromatic complex.

In difference to the mechanism for $(\bar{1}012)$ twins, where the vectors belong to the dichromatic pattern. Further the $(b, 2h_0)$ TDs have a greater mobility in $(\bar{1}013)$ and $(\bar{1}011)$ twins as $(b, 4h_0)$ TDs. Another explanation why the $(\bar{1}011)$ and $(\bar{1}013)$ twins can only be activated under pressure is the impossibility of moving the TDs in anti-twinning sense [27].

Kiener *et al.* [1] conducted a tensile test on high-purity Mg with a sample size $4\ \mu m$. The crystal orientation [0001] was selected, as this favours the activation of tensile twinning. At a constant flow stress of approximately 80 to 90 MPa an elastic-plastic transition is observed, which corresponds well to the nucleation and growth of a tensile twin.
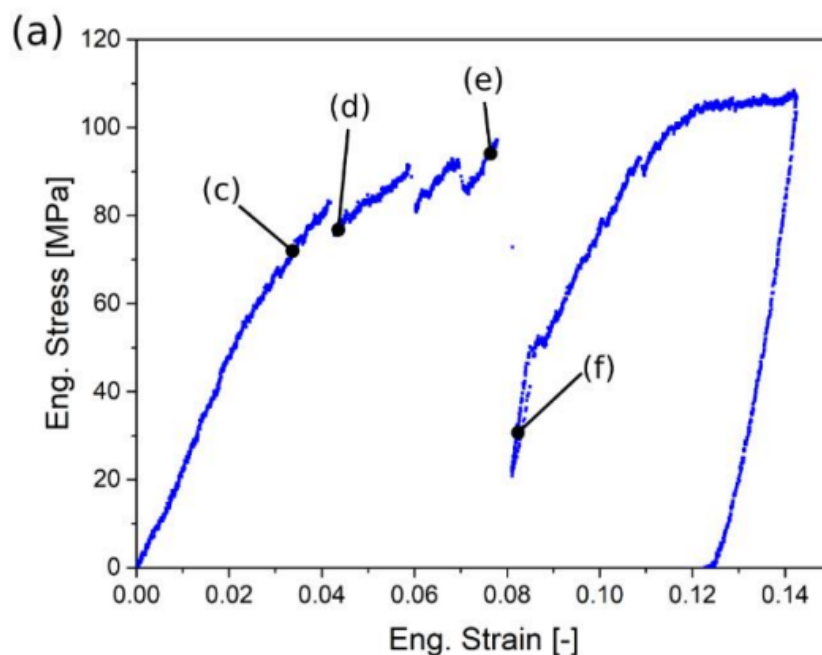
Figure 10: Stress-Strain-Curve of tensile test of Mg, adapted from [1]

The first nucleation of a twin can be noticed in Figure 10 [1] at a strain of 0.04 and the second at 0.08, which can be identified by the pronounced load drop at 0.08.

In magnesium, two different twins can occur along the [0001] direction, the $(\bar{1}012)$ tensile twin and the $(\bar{1}011)$ compression twin, where the compression twin rarely forms because it has a relatively high activation energy. By slightly twisting the tensile specimen, the compression twin may also have been activated, but it is more likely that the tensile twin will nucleate under this loading. The compression twin is crystallographically favoured by the tensile load, but its occurrence is unlikely at a CRSS of 90 MPa, as much higher stresses would be expected, as depicted in Figure 4. It is suspected that a twin has formed in the twinned part. An important point is that the threshold for twinning does not seem to be constant.

18

These in turn depend on the state of the local stress and strain and cannot always be derived from the value of the global stress. Notably, a compression test was also performed with a $2\ \mu m$ specimen.

Comparing the CRSS for tensile and compression twinning, it is evident that the required nucleation stress for the $2\ \mu m$ compression configuration is about 250% larger than that of the $4\ \mu m$ tensile configuration. This could be attributed to a potential size effect, among other things, but for this large difference this influence should be too slight.

Therefore, not only the CRSS was taken into account, but also the strain. The strain in the tensile sample is $\varepsilon =\ 0.00173$ and for compression $\varepsilon =\ 0.00298$, which is an increase of about 60% for a reduction in size by a factor of two. It was therefore concluded that the formation of tensile twins is dependent on strain rather than stress [1].

2.5. Deformation behaviour of Zn

Slip in Zn crystals occurs mainly on the most densely packed basal plane $\{0001\}$ in the $<1\bar{2}10>$ direction. Furthermore, slip can occur along the secondary pyramidal plane $(11\bar{2}2)$ in $<11\bar{2}3>$ direction. For basal slip, two linear independent $<1\bar{2}10>$ directions and five linear independent $<11\bar{2}3>$ directions can occur on the secondary pyramidal plane [28], [29]. As stated before the $\{10\bar{1}2\}$ twin occurs as a compression twin for Cd and Zn ($c/a > 1.73$), since the shear direction for the $\{10\bar{1}2\}$ twin reverses at $c/a = 1.73$ [4].

Therefore, it can be observed that Zn single crystals take up $6\ to\ 8$ times more plastic strain in compression than in tension, this difference is attributed to $(10\bar{1}2)$ twinning as a result of compressive strain along the c-axis [4].

Deformation kinking is another deformation mode which is less common when compared with slip and twinning but is important for materials with high plastic anisotropy. The formation of deformation kink bands is found in many anisotropic materials. Further these deformation kink bands can form in materials where only one slip system is predominant. In one of the first models to explain deformation kinking in hcp-crystals, Zn single-crystals were used as depicted in Figure 11 [30]. The model suggests cooperative initiation and/or operation of the basal dislocations, followed by arrangements of basal dislocations which align perpendicular to the
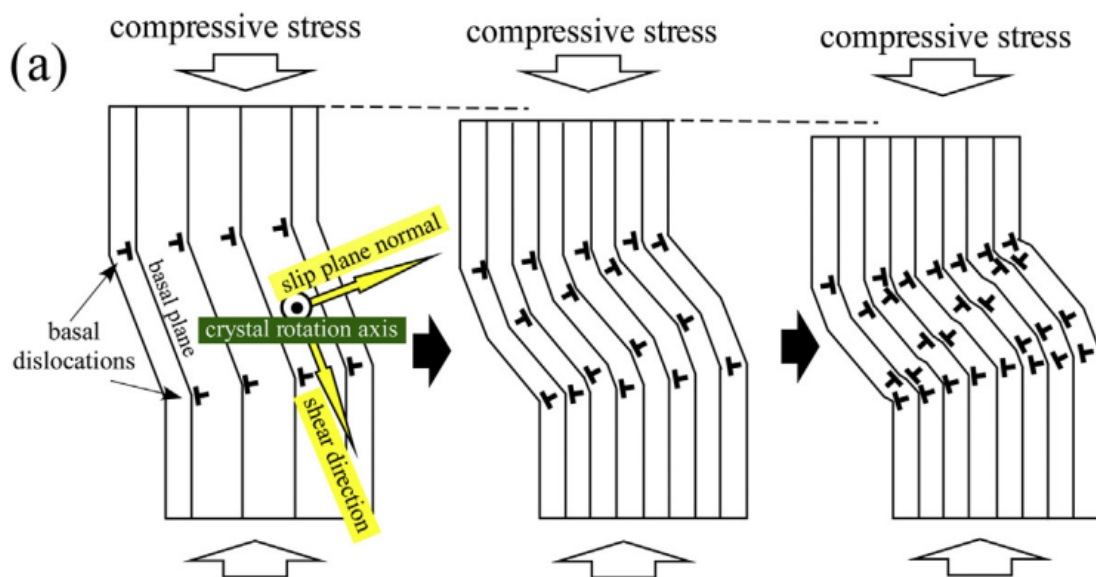
Figure 11: Deformation kink band model for Zn single crystal, adapeted from [30]

slip plane. This process is believed to be the basic process for deformation kink band boundary. The crystallographic natures of deformation kink bands have not been completely clarified

Washburn *et al.* [30] found conditions where deformation kink bands developed under tension. One factor is the nonuniform tension along the gauge length combined with the restraint imposed by the tensile load. Some factors mentioned which may have caused differences in flow stress along the length of the crystals are, for example, irregular distribution of impurities, accidents of growth (lineage structure), damage during handling, surface conditions, and strain-aging characteristics because of dissolved nitrogen. When plastic flow once started in a local region, it continued often up to high strain before other parts of the gauge became active.

3. Experimental

Two hexagonal materials with different c/a-ratio were selected for the experiments: Zn and Mg. The materials were all single crystalline and technically pure (99.999%). Six tensile specimens were fabricated from each of these materials. Two of each of these samples were designed to have nominally the same dimensions, namely $2, 4$ and 6 μm in gauge width, respectively as depicted in Figure 12.
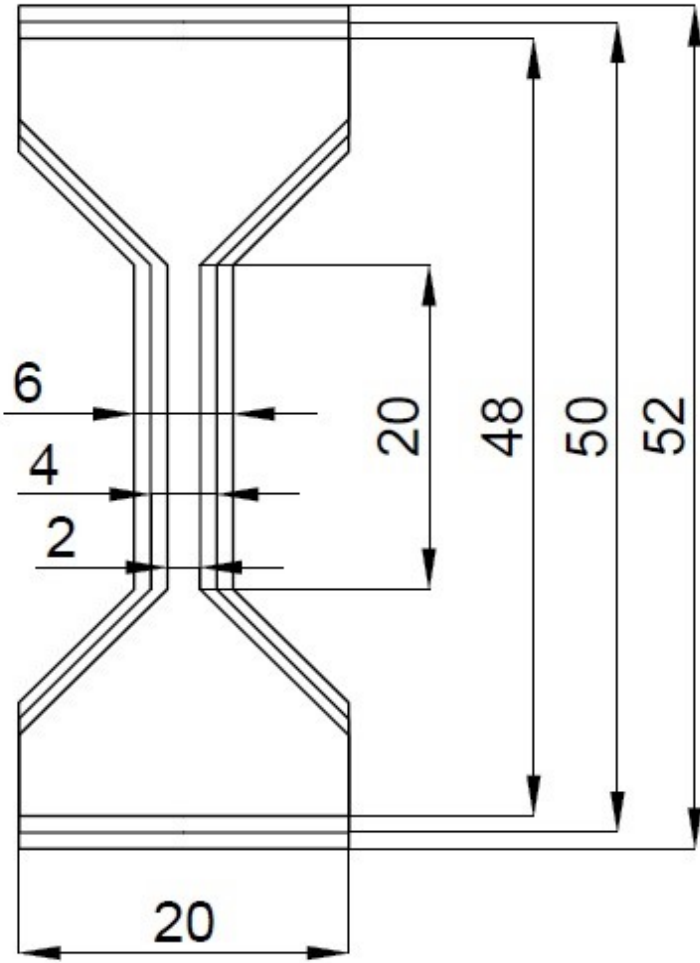
Figure 12: Sketch of the samples with the change in geometric dimensions

3.1. Metallographic preparation

Initially 1.5 mm thick plates with approximate dimensions of $3 \, x \, 3 \, mm$ were first cut out of the single crystals with a cooled diamond wire saw. The orientation of the crystal was marked to make sure, that the tensile specimens will be oriented in [0001]. It is important to work with as little pressure as possible, to prevent the material from deforming. In the next step, thin lamellae were grounded or etched so that the tips of the samples were approximately 20 μm thick. Therefore, the Mg sample was etched with citric acid, whereas the Zn sample was etched electrochemically using the commercially available electrolyte A2.

3.2. Focused ion beam milling

For micron scale specimen fabrication, a FIB of type Zeiss Leo 1540XB (Carl Zeiss AG, Oberkochen, Germany) was used. The Mg sample was mounted and processed in the FIB directly after the metallographic preparation. In Figure 13 the first steps for thinning out the Mg lamella can be seen.
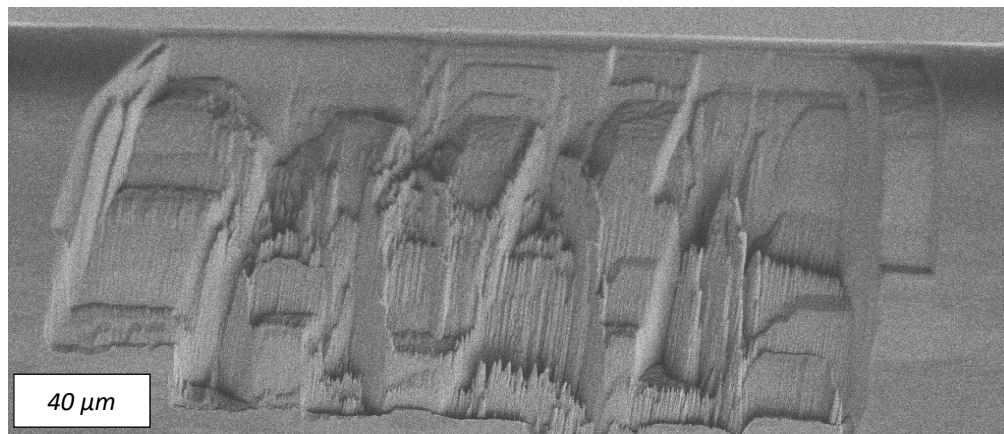
Figure 13: First rough cuts on the etched lamellae made for Mg

The Zn lamella was laser cut in advance to reduce fabrication time. A femtosecond laser unit (OneFive Origami, NKT Photonics Switzerland GmbH, Regensdorf, Switzerland) mounted inside a FIB/SEM Auriga workstation (Carl Zeiss AG, Oberkochen, Germany) was used for pre-processing the samples [31]. The aim of the laser cutting was to pre-cut beams which only need to be trimmed and thinned, these cuts are visible in Figure 14.

In the first step of the Mg preparation, a 320 μm long and 40 μm micrometer deep lamella was cut out of the sample using a Ga^+ current of 10 nA. The ridge width is approximately 10μm. In the next step, bars with a width of 20 to 25μm are machined into the thinned-out area.

For the preparation of Zn, these steps were omitted. To achieve the desired thickness, the specimen was rebuilt and mounted upright, allowing the side surfaces to be thinned, using a Ga^+ current of 1 nA, and subsequently polished using a Ga^+ current of 500 pA. It is important to create a smooth surface that is as free of defects as possible to see evident changes on that during *in situ* mechanical experimentation.
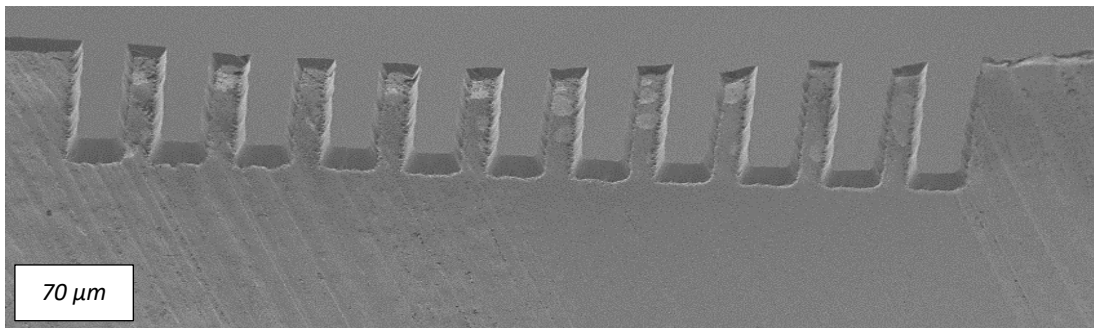
Figure 14: Zn lamella after pre-laserprocessing

In the next step, the specimens were cut into rectangles as depicted in Figure 15a. As already mentioned, two samples of each material were created with the gauge widths and heights of 2, 4 and 6 μm, respectively. The gauge length is 20 μm for all samples.
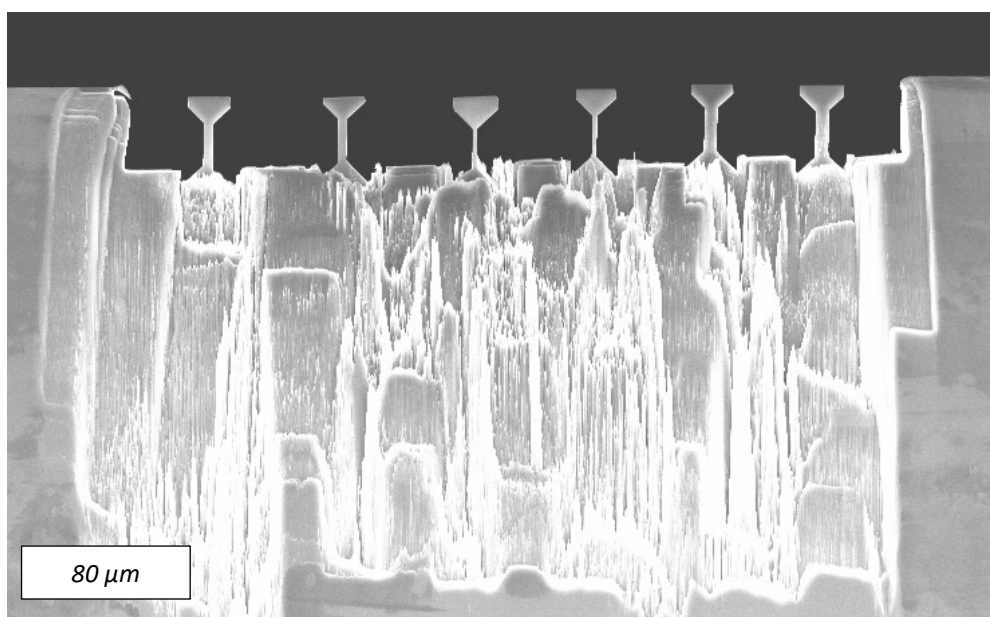
Figure 15: Overview of the finished Mg samples
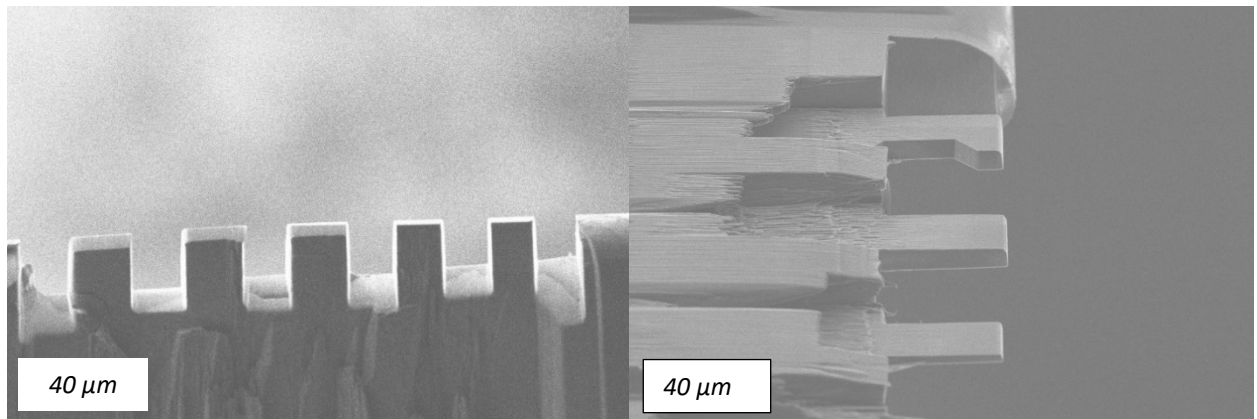
Figure 16: a) Rough cut rectangles in the lamella and b) subsequent forming of the samples

From Figure 15 to Figure 16 the individual process steps of the Mg samples up to their final shape can be observed.

3.3.Sample testing

To determine the exact geometry of the samples, images were taken in advance of the tensile tests with another SEM (Leo 1525, Carl Zeiss AG, Oberkochen, Germany). Afterwards the images were analyzed with the program ImageJ (ImageJ 1.53k). The samples were subsequently tested in situ inside an SEM (DSM982, Carl Zeiss Ag, Oberkochen, Germany) using an UNAT-SEM 1 (ASMEC GmbH, Dresden, Germany) microindentation device with a gripper constructed of tungsten as shown schematically in Figure 17.
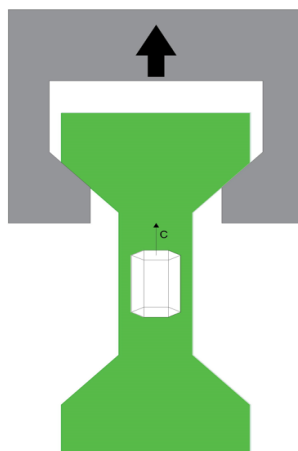
Figure 17: Arrangement of the sample, the gripper and the schematic orientation of the crystal

Sample testing

The aim was to align the sample so that it is loaded along the c-axis. This arrangement is schematically depicted in Figure 17.

The samples were strained to about 20% at a nominal strain rate of $10^{-3}s^{-1}$. The test lasts a total of $400\ s$, with $200\ s$ of loading and $200\ s$ of unloading, respectively. After the test, detailed images were taken again to have a close look at sample deformation. During the test, load, time and displacement were measured. In the evaluation, an engineering stress-strain curve is calculated from the load-displacement data, utilizing Equation 6:

$$\sigma = \frac{F}{A}$$

Equation 6: Calculation of the engineering stress

Here the F stands for the load, A is the area and σ is the engineering stress. The engineering strain is calculated by relative displacement Δl over initial length l, as:

$$\varepsilon = \frac{\Delta l}{l}$$

Equation 7: Calculation of the engineering strain

4. Results and Discussion

In the following chapter the results of the tensile tests are presented for all specimens that where oriented to beloaded in [0001] direction under tension.

4.1.Dimensions of the samples

The following table summarizes the measured specimen dimensions. The specimen names correspond to gauge width and sequence number.

Mg	gauge length[μm]	gauge width [μm]	thickness [μm]	area [μm²]
6-1	21.36	5.93	5.99	35.48
6-2	20.12	6.23	5.74	35.79
4-1	20.56	4.14	3.89	16.08
4-2	19.32	4.20	4.07	17.10
2-1	18.77	2.35	2.35	5.50
2-2	18.58	2.16	2.04	4.40

Table 2: Dimensions of the Mg samples before testing

Zn	gauge length[μm]	gauge width [μm]	thickness [μm]	area [μm²]
6-1	19.14	6.48	6.23	40.41
6-2	19.57	6.36	6.11	38.85
4-1	21.05	4.26	3.40	14.46
4-2	20.56	4.26	3.77	16.04
2-1	21.48	1.91	2.16	4.13
2-2	22.78	2.04	1.60	3.27

Table 3:Dimensions of the Zn samples before testing

1. Tensile tests of the Mg samples

Before the samples were tested, an EBSD measurement, depicted in Figure 18, was taken to check that they were correctly oriented. Unfortunately, it had to be realized that some twinned regions (red area in Figure 18) had already formed prior to testing, during lamella manipulation. Therefore, it cannot be guaranteed that the samples are completely sc. This in turn would have an influence on the later deformation and the values that could be recorded during the tensile test. In order to be able to make a statement about the CRSS of the Mg samples and to interpret the behaviour to some extent, it is assumed that the samples were loaded in the preferred [0001] direction and that the samples are sc. This bears a certain uncertainty, but offers a possibility to compare the determined values with values from literature.
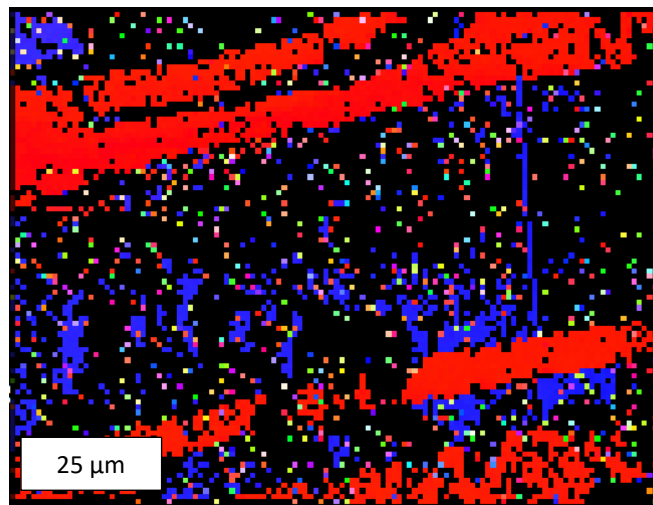
Figure 18: EBSD-measurement of the Mg before testing

Tensile tests of the Mg samples

Figure 19 shows all recorded and subsequently converted stress-strain curves for the Mg samples.
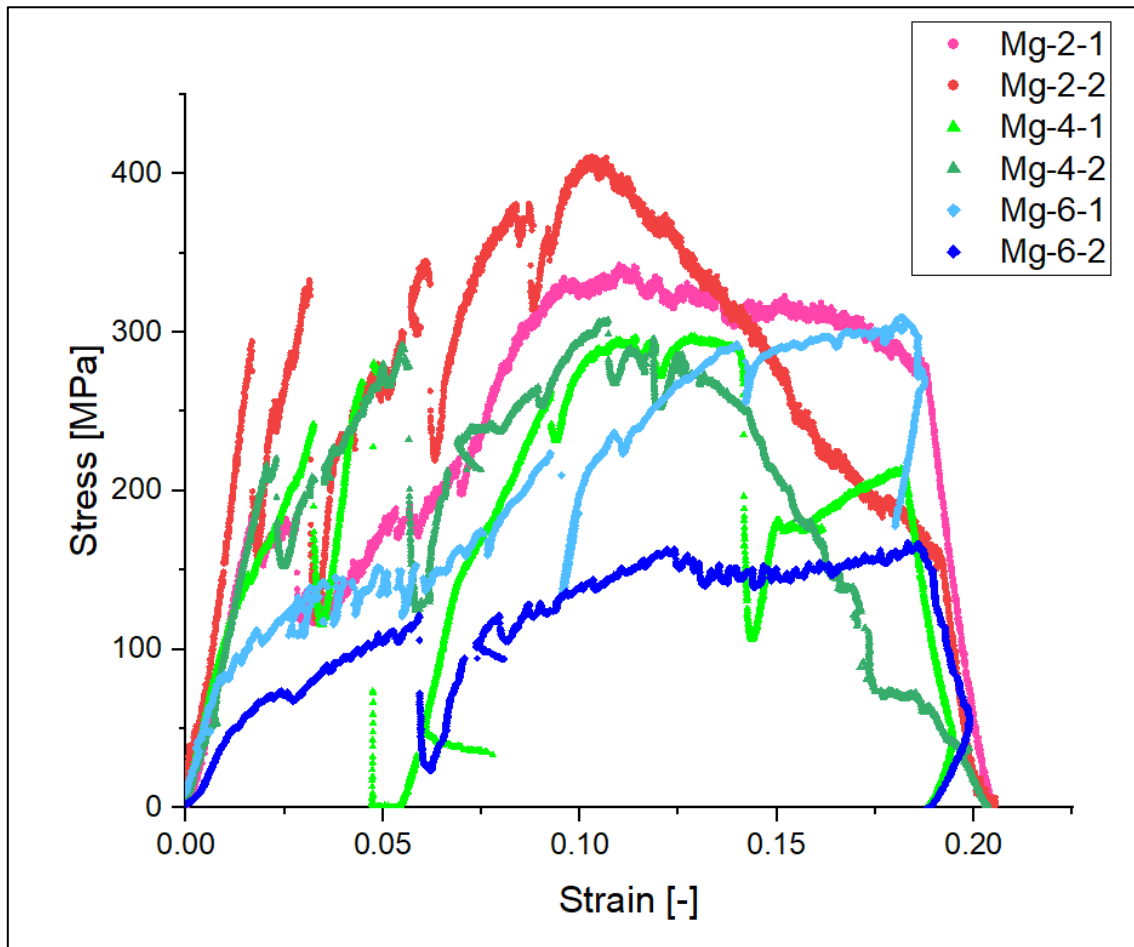
Figure 19: All stress-strain curves of the Mg samples

A trend in favour of the size effect is evident. Increased yield strength can be observed in the smaller samples. Some significant differences can be observed between the samples of the same size. Keep in mind that among the influencing factors that explain these differences could be the fact that the samples were already twinned before the experiment and therefore the same crystal orientation of the specimens cannot be guaranteed. Besides considerations such as stochastics and statistics of dislocation sources.

In some samples hardening can be observed, which is justified by the increase of the stress after the yield-point. For example, in sample Mg-6-1, the stress continues to increase until unloading occurs and the force is removed. This can also be observed in other samples, but not as pronounced. In order to compare the hardening behaviour of the samples, the strain hardening rate SHR was calculated. The stress drops, but then rises again to the previous level and then rises further.

Tensile tests of the Mg samples

The SHR was calculated with the following equation adapted from [32] and is listed in Table 4:

$$SHR = \frac{\Delta\sigma}{\Delta\varepsilon} = \frac{\sigma_{0.1} - \sigma_y}{\varepsilon_{0.1} - \varepsilon_y}$$

Equation 8: Calculation of SHR, adapted from [30]

When looking at the curves and comparing them with the results of the SHR, a clear correlation can be seen. As depicted in Figure 20, the SHR increases for small samples, especially when comparing the Mg-2 samples with the Mg-4 samples, which again speaks for a size-effect. However, the Mg-6 samples again show higher SHR than the Mg-4 samples, which could be due to the formation of a thick oxide layer on these samples, which prevents the dislocations from leaving the crystal. Mg-6-1 in particular has a high SHR, this also fits with the curve.
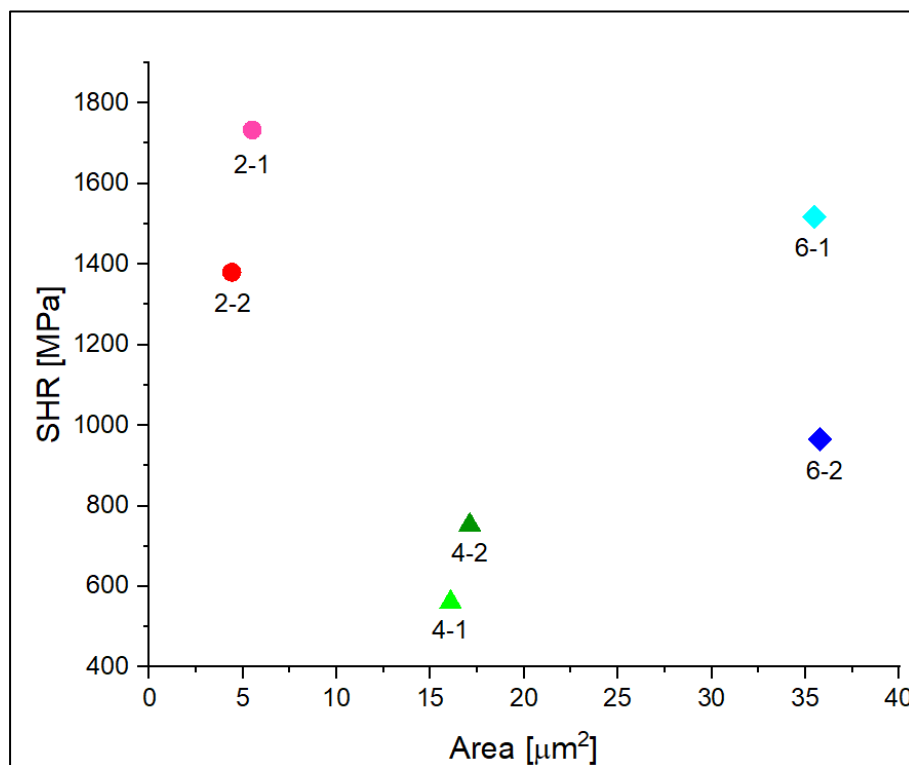
Figure 20: Represantation of the SHR over the area

Another influence on the hardening behaviour is the number of dislocations that were introduced during the preparation. However, to assess the dislocation density of the samples, further investigations would be required.

The calculation of the CRSS was based on the Schmid factor m of Kiener *et al*. [1]. Due to the loading along the c-axis, it is only possible to cause pyramidal $< c + a >$ slip, $\pi1$ $(m = 0.4) and$ $\pi2$ $(m = 0.45)$, or tension twinning $(m = 0.5)$ [1]. Here, the stress was used at which the elastic range changes into the plastic range. The specimen Mg-6-2 is the only one to show an abrupt elongation indicating a twin, occurring at a strain of 0.059 and drops from $120\ MPa$ to $24\ MPa$. The CRSS for the formation would be $60\ MPa$.

In the study by Kiener *et al.* [1] the CRSS for the formation of a tension twin is about $50\ MPa$ for a sample with $4\ \mu m$ dimension, which is in the same range as the calculated CRSS for the sample Mg-6-2, but it has to be taken into account that Mg-6-2 has a larger area and thus the value should theoretically be lower than the comparison value.

However, this comparison is not completely valid, as the orientation of the sample was not certain and there is also the possibility that the sample has been twinned before.
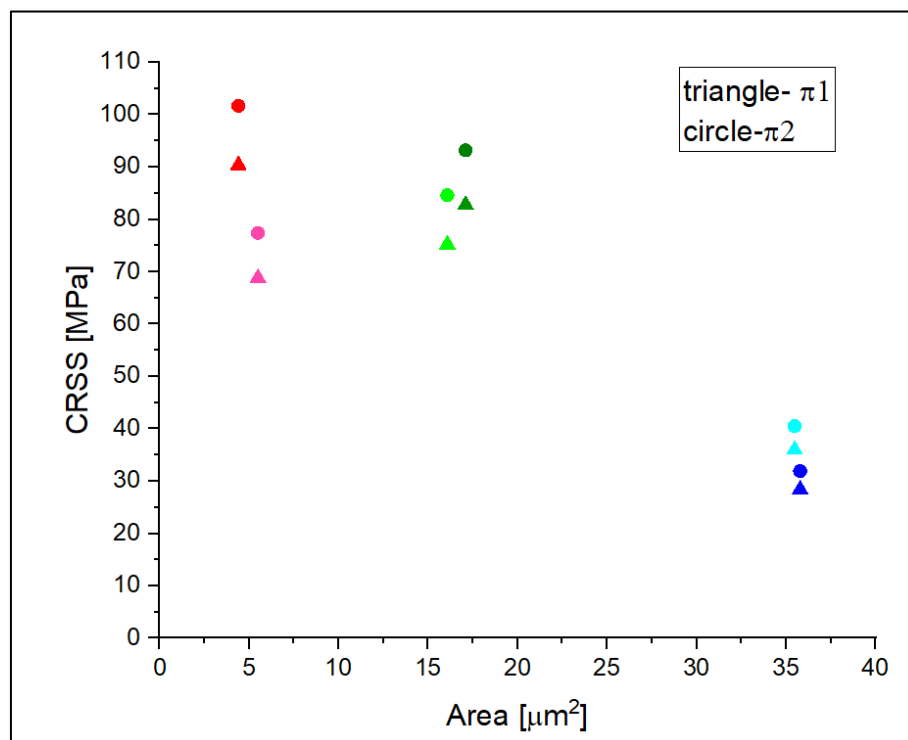
Figure 21: Representation of the CRSS over the area

Jeong *et al.* [20] have listed the CRSSs for sc Mg pillars for different types of deformation, here the CRSS for pyramidal $\pi2 < c + a >$ slip is $80\ MPa$. In Figure 4 [11] CRSSs for different deformation mechanisms are depicted. The CRSS for pyramidal slip there ranges from about $30 MPa\ to\ 75\ MPa$, which is in the same range for all samples except Mg-2-1.

These CRSSs must be considered critically, but again show that more stress must be applied for a smaller sample size, depicted in Figure 21. The values are generally below those previously discussed by Kiener *et al*. [1]. As reported by Dimiduk *et al.* [23] in their work, higher strength and CRSS values occur in pillars with a diameter of less than $\sim 16 \ \mu m$. This assumption can also be transferred well to these values, as there is a significant increase between the CRSS values of the Mg-6 samples and the rest of the samples.

The Young's modulus for the specimens was only calculated by the linear evaluation of the elastic range, whereby the compliance of the gripper, and the setup, is still included in the result and thus leading to overall lower bound result. Therefore, a comparison with values from the literature is hardly possible.

Kiener *et al.* [1] calculate a Young`s Modulus of $\sim 40 \ GPa$, for a tensile test sample with the same arrangement as presented in this study and with a diameter of $4 \ \mu m$. This is nearly four times higher as in the presented experiments, here the apparent modulus is between $8.6 \ and \ 11.1 \ GPa$.

Tensile tests of the Mg samples

In Table 4 the evaluated mechanical properties of the Mg samples are listed.

	Mg-6-1	Mg-6-2	Mg-4-1	Mg-4-2	Mg-2-1	Mg-2-2
max.stress [MPa]	303 ± 3.9	163 ± 1.6	290 ± 4.5	290 ± 17.3	336 ± 2.7	405 ± 2.3
App. elastic modulus [GPa]	8.2	4.6	8.6	11.1	11.8	19.2
yield stress [MPa]	90 ± 2.9	71 ± 1.0	188 ± 48.8	207 ± 4.0	172 ± 5.5	226 ± 54.3
CRSS $\pi1$ [MPa]	36± 1.2	28± 0.4	75± 19.5	82± 1.6	68± 2.2	90± 21.7
CRSS $\pi2$ [MPa]	40± 1.3	31± 0.45	84± 22.0	93± 1.8	77± 2.5	101± 24.4
Strain hardening rate (SHR) [MPa]	1518	966	561	753	1733	1380

Table 4: Mechanical properties of the Mg samples

4.1.1. Results from Mg-6

In Figure 22 the stress-strain curves of sample Mg-6-1 can be seen. Through the images taken during the experiment, the significant points or sections in the curve, marked with letters, can be assigned to an event during the deformation.

There are several stress-drops visible in each curve, which abrupt changes can be assigned to. The transition from the elastic to the plastic range is around 0.001, a small deviation from linear elasticity can be observed before this, but the stress continues to increase linearly afterwards with the same gradient. The yield stress is at $90\ MPa$. First changes are evident at about 0.02 elongation *(a),* the drop at 0.05 *(b)* can be assigned to further crack formation. At a strain of 0.07 the crack at the base appears. The largest stress drop in the curve is at 0.1 *(c),* upon which the stress decreases by about $100\ MPa$, this event can be aligned to the widening of the cracks which formed at a strain of 0.07. One last larger drop *(d)* can be assigned to the kink in the head of the sample. As mentioned before, hardening can be seen in this sample. Although the stress keeps falling stochastically, the overall trend continues to rise.
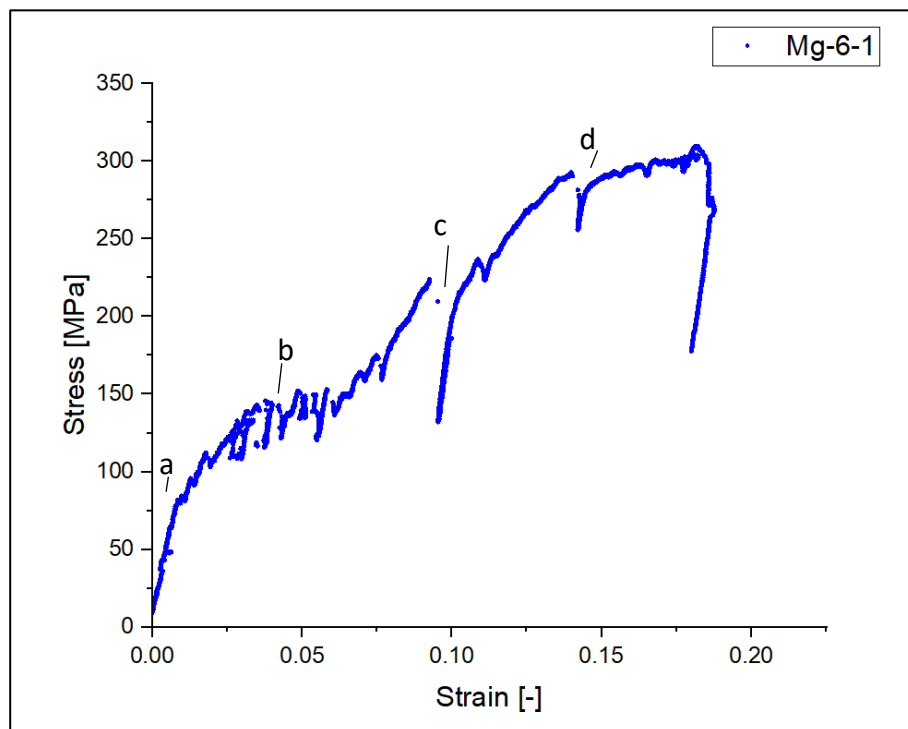
Figure 22: Stress-strain-curve of the sample Mg-6-1

Results from Mg-6

Figure 23 shows the images recorded during the experiment which can be assigned to the characteristic points in the curve.
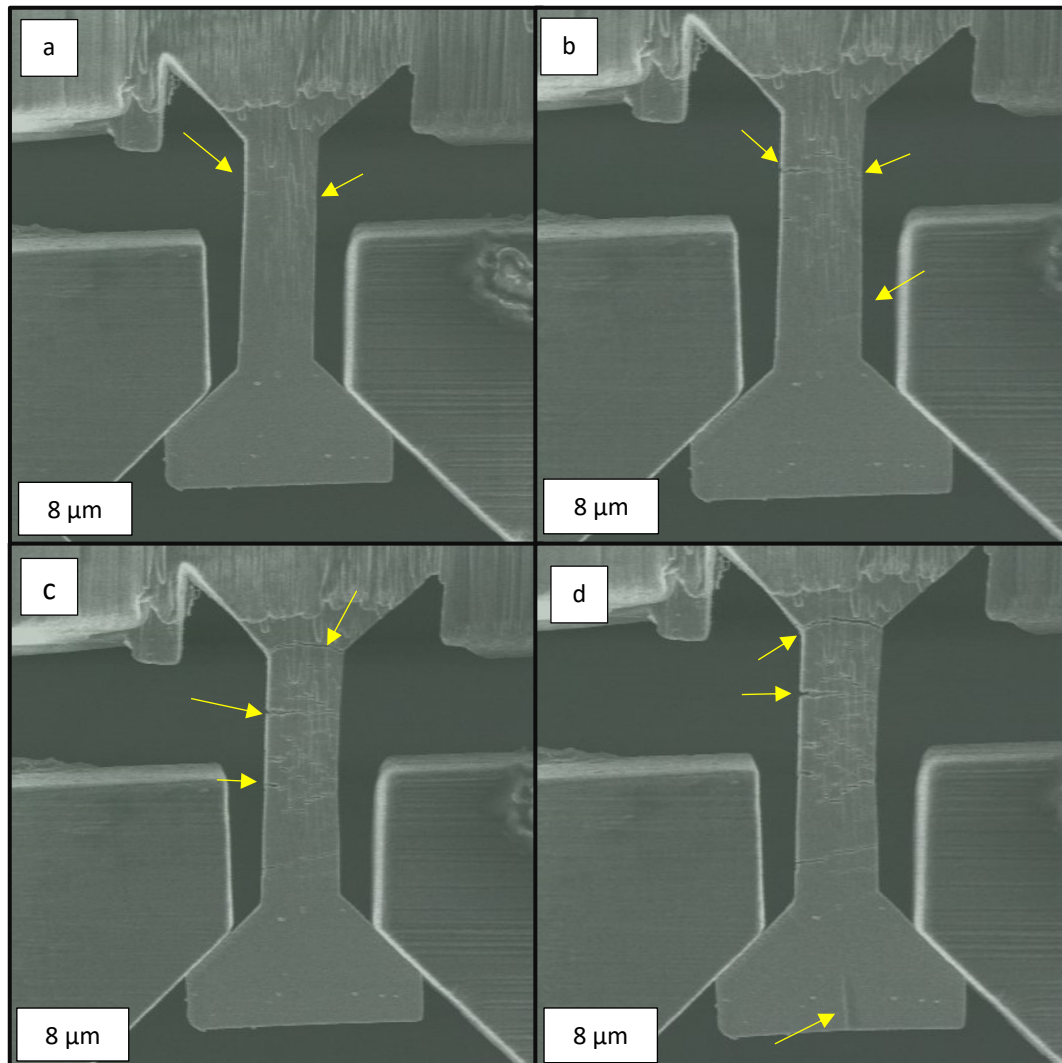
Figure 23: Images taken while testing sample Mg-6-1, the yellow arrows mark the cracks

The many small cracks cannot be clearly assigned, but a widening can also be observed the higher the strain becomes. It seems that the crack at the base and the crack underneath (Figure 23d) have the greatest influence. Furthermore, it is likely that these cracks are formed only on the surface oxide layer, which is very pronounced in Mg, but do not traverse the entire metallic specimen inside, initially. When measuring the gauge-length before and after the experiment, it could be found that there was a plastic deformation extension of 6.4% for Mg-6-2 and 8.9% for Mg-6-1. The remaining elongation, of the 16% depicted in Figure 22, is attributed to the deformation of the head.

The maximum stress of the samples differs almost twofold, with a Max. Stress of $163\ MPa$ for Mg-6-2 and $303\ MPa$ for Mg-6-1.

It could be that the slight misalignement in Mg-6-1 as depicted in Figure 25 lead to a superposition of bending and tensile loading which resulted in overestimation of the strength.

When comparing the two samples, depicted in Figure 24, a similar course of the stress-strain curves can be observed, both show strain hardening, but as mentioned Mg-6-1 rises to higher s stresses and shows higher strain hardening, which is also supported by the SHR.
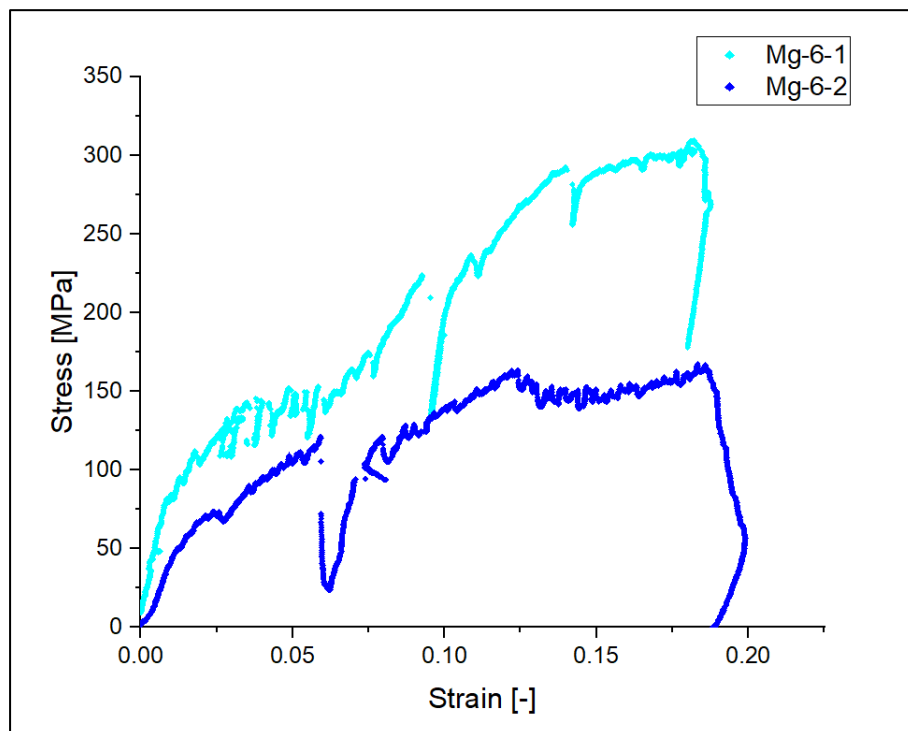
Figure 24: Comparison of the stress-strain curves of Mg-6-1 and Mg-6-2

Another influence on the deformation behaviour and also the appearance of the cracks could be the thickness of the oxide layer. A source for the thicker oxide layer might be that the surface of Mg-6-1 was rougher because it was polished less in the FIB. Due to this roughness, there is more surface area and the oxide layer can develop easier. It is assumed that the oxide layer on sample Mg-6-1 is thicker compared to other samples, which could explain both the increased strength and the higher strain hardening. Due to the increased thickness, the layer does not crack immediately over the entire sample, but small cracks appear which then move in a staircase manner over the sample. Because of the thicker oxide layer, it is also possible that the dislocations cannot escape from the crystal and thus lead to higher strain hardening.

Results from Mg-6

The sample in Figure 25 looks bent, this could have occurred because the sample was not completely symmetrical, which also explains the staircase-shaped cracks.
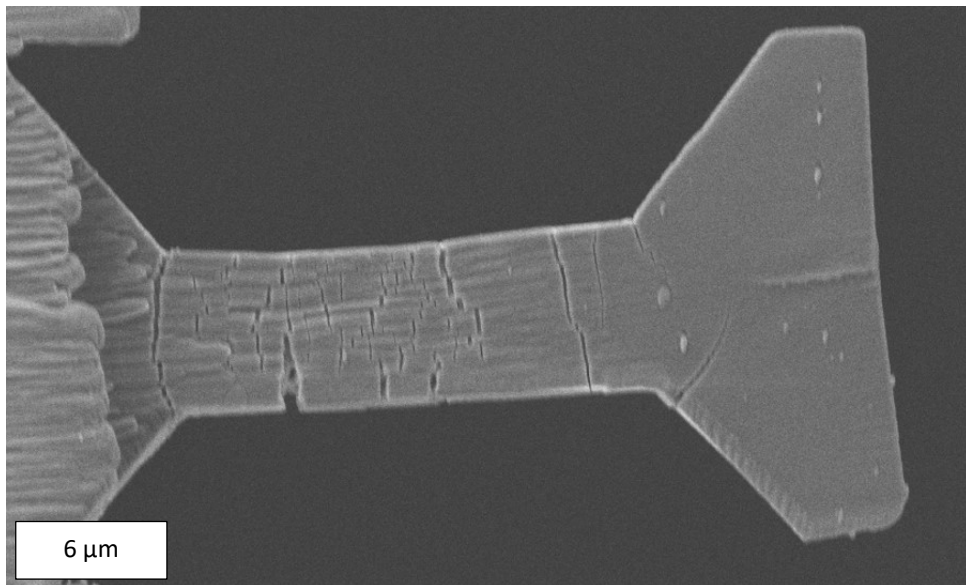
Figure 26: Image taken of Mg-6-1 after the experiment

The comparison with MG-6-2 is not valid for a strain in excess of 0.14, because the head of the sample starts to slip and thus most of the deformation takes place in there and the stress decreases due to the instability, depicted in Figure 26. This was caused by the load exerted by the gripper on the contact surface of the sample. This could have activated a slip system which caused the whole head to slip off.
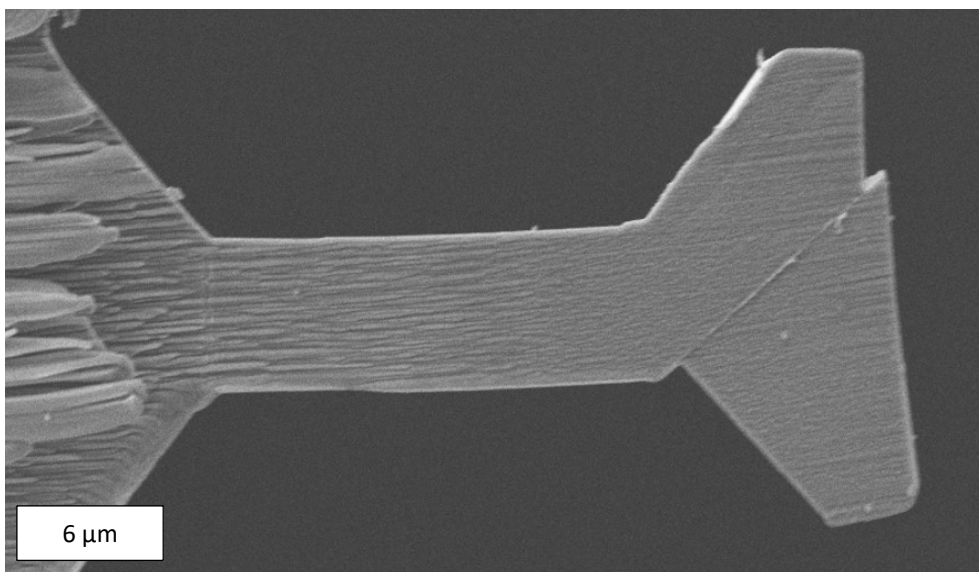
Figure 25: Image taken of Mg-6-2 after the experiment

4.1.2. Results from Mg-4

In Figure 27 the stress-strain curve of the sample Mg-4-2 can be seen. The prominent points and sections of the curve are again marked with letters.
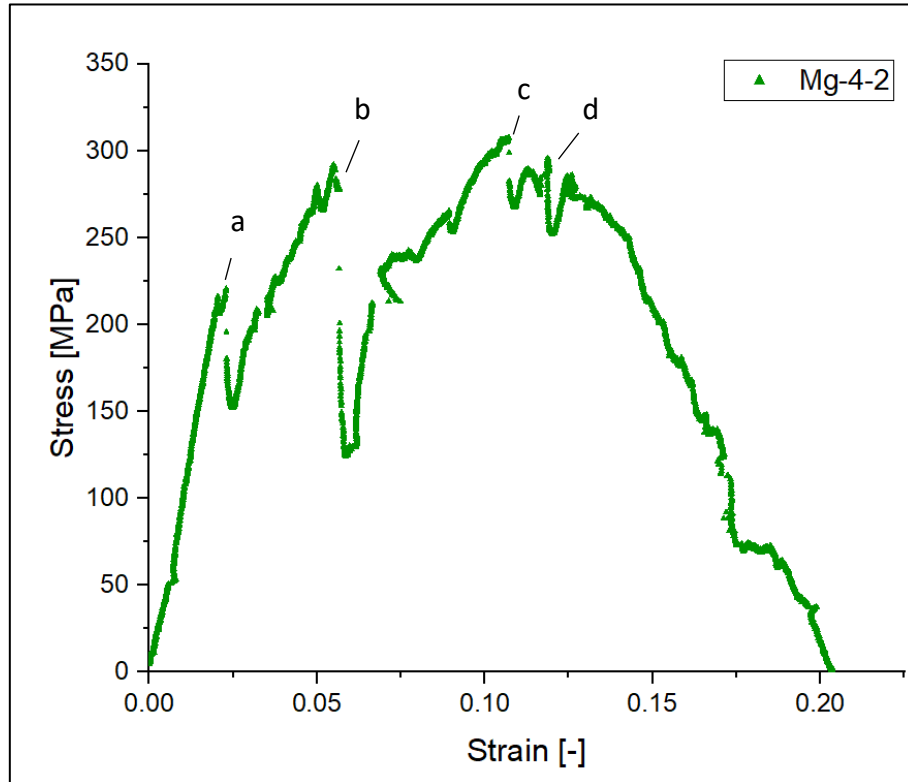
Figure 27: Stress-strain curve of Mg-4-2

The transition from the elastic to the plastic range can be observed at an elongation of about 0.03, the value of the yield stress is 204 MPa. At a strain of 0.035, a sudden elongation can be observed in the sample, which is not visible on the surface but causes a stress drop of about 60 MPa. This feature could likely be the nucleation of a twinned region inside the specimen. The first cracks can be observed at an elongation of *0.04 (a)* on the images taken during the experiment. The stress drop at a strain of *0.06 (b)* can be attributed to a crack at the top of the base. From a strain of *0.1 (c)* onwards the stress increases, from 240 to over 300 MPa, many small cracks become visible and the crack at the base starts to widen. Less strain hardening can be seen in this sample. The stress increases slightly up to 0.1, but much less compared to MG-6-1. Past an elongation of *0.12 (d),* the crack widens even further and faster.

Results from Mg-4

As the crack finally ruptures, the stress decreases quickly. In comparison with the ductile ruptured volume, evident in Figure 28d, the visible straight crack front is another indicator that crack formation arises in the oxide layer and not in the metallic region of the specimen.
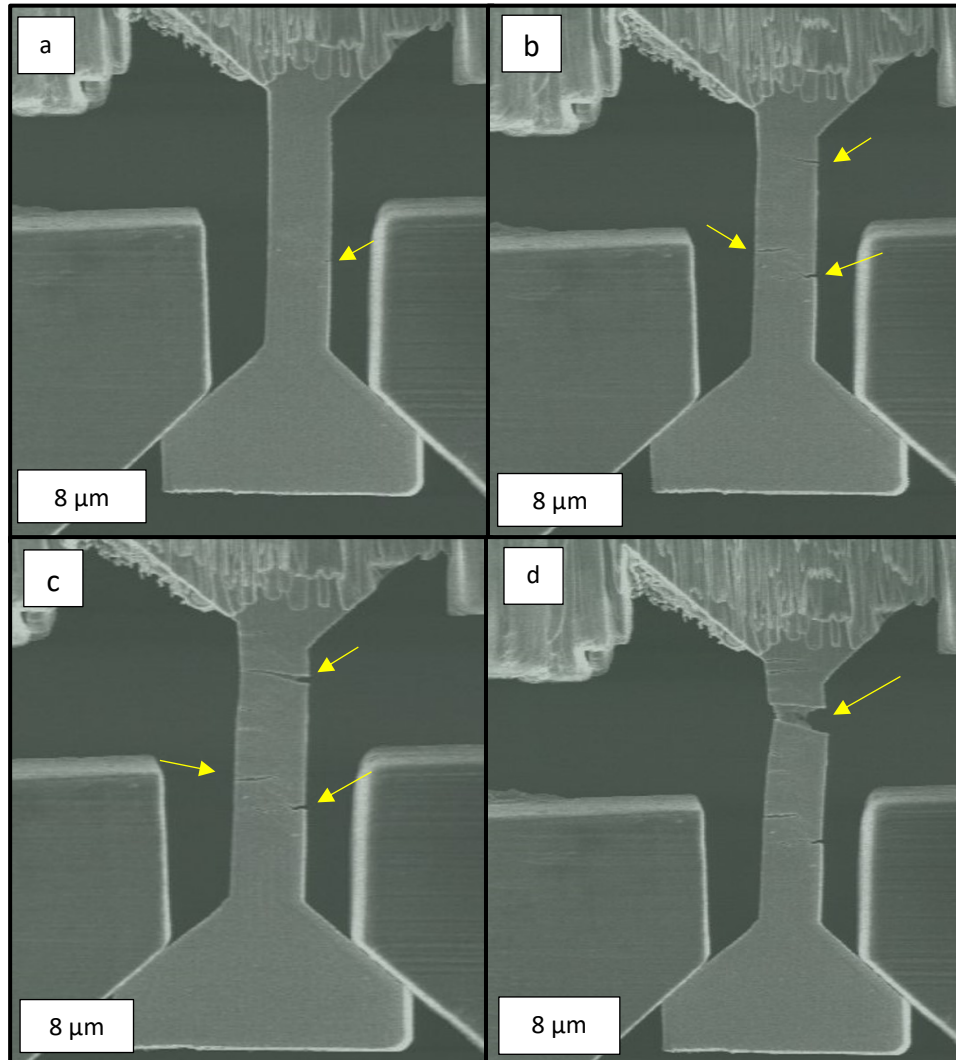
Figure 28: Images taken while testing Mg-4-2, the yellow arrows mark the cracks

In Figure 28d it seems as if the sample would break, but this does not happen, and the sample could be mounted in another SEM after the experiment to observe the damage even more precisely. It seems that the cracks that formed in the oxide layer could have spread further into the Mg and thus cause rupture of the metal.

The elongation of the gauge section was measured, here a plastic deformation of 8.9% was found for Mg-4-1 and 13.4% for Mg-4-2. In Figure 29 the comparison of the two samples Mg-4-1 and Mg-4-2 is depicted. It must be noted that Mg-4-2 almost tore completely during the experiment.

Results from Mg-4

In Mg-4-1, the head of the specimen is strongly deformed, but this may also be due to the unfavourable geometry, as the head was too short, which could lead to a major contribution of bending stresses outside of the gauge section.
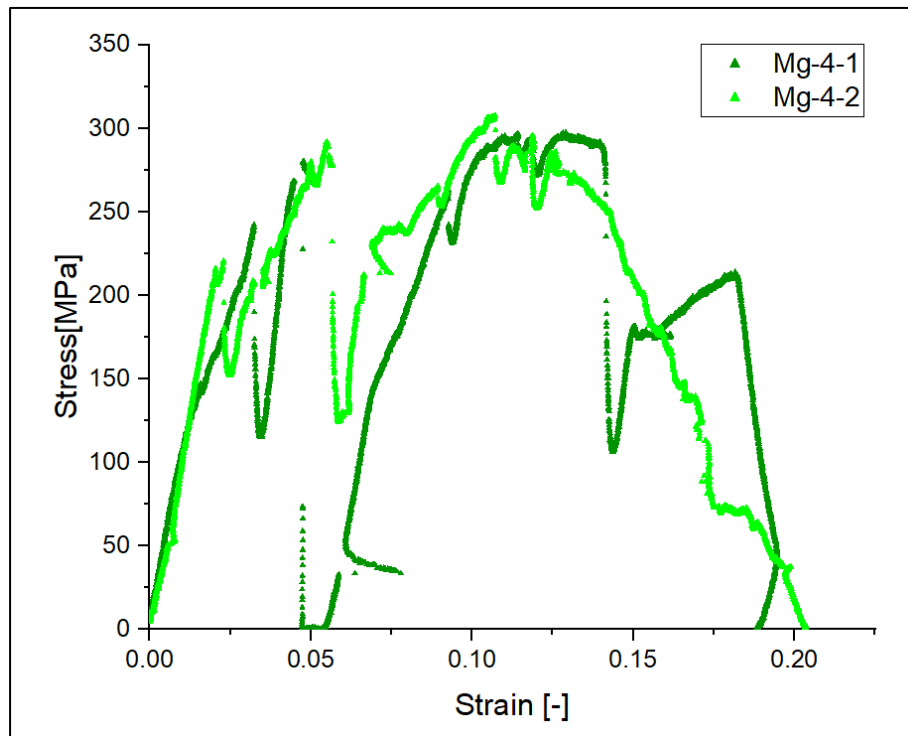
Figure 29: Comparison of the stress-strain curves of Mg-4-1 and Mg-4-2

Regarding the data of Mg-4-1, the stress drops are more pronounced and once even go down to zero. As mentioned before, each stress drop can be associated with the formation of a surface oxide crack. For Mg-4-2, the stress decreases continuously after the highest stress has been reached, which is due to the significant damage of the sample. Apart from this, the characteristics of the two curves appear similar.
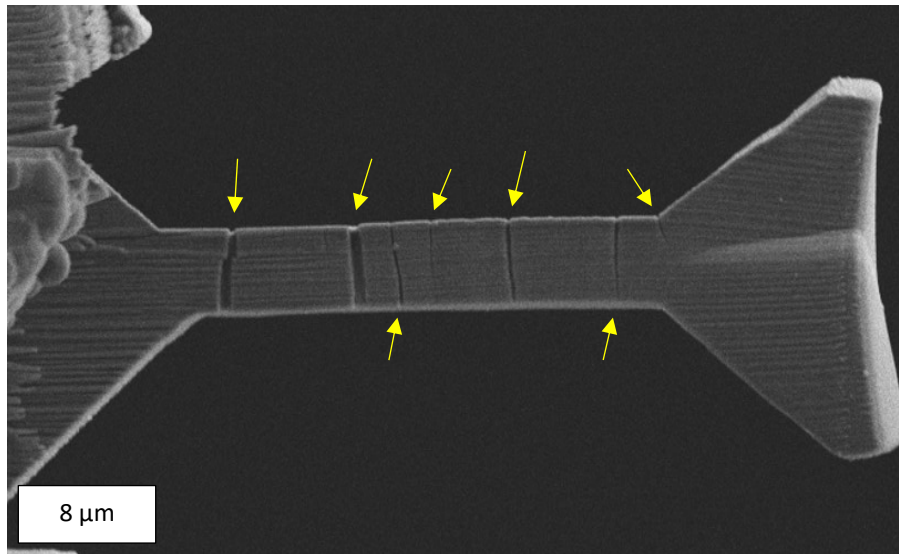
Figure 30: Image taken of the sample Mg-4-1 after the experiment

In Figure 30 the cracks in the oxide layer, which have spread perpendicular to the direction of the load, can be seen. These always run across the entire gauge width, unlike in the previously discussed Mg-6 samples on which smaller cracks have formed. As the Mg-4-2 sample is almost completely cracked, it is possible to estimate the thickness of the oxide layer because the fracture surface is visible. The close-up look of the crack is depicted in Figure 31 and it appears that the surface area of the sample behaves rather brittle, stating the formation of a thick oxide layer. Below this layer, the specimen surface looks rather ductile, suggesting metallic Mg. The thickness of the oxide layer is estimated to be between $150\ and\ 200\ nm$. The layer on the bottom of Figure 31 is probably due to redeposition during preparation in the FIB.
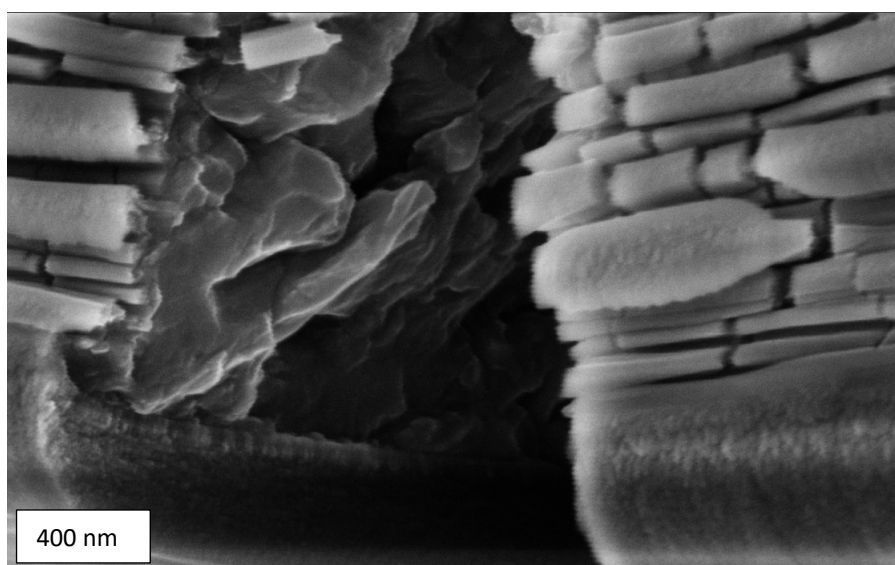
Figure 31: Close-up view of the fracture surface of Mg-4-2

4.1.3. Results from Mg-2

The following stress-strain curve, Figure 32, is the one with the highest stress and the one with the smallest dimensions, which again fits the size effect. Damage to the sample was also clearly visible in this experiment and can therefore be assigned to various points on the curve.
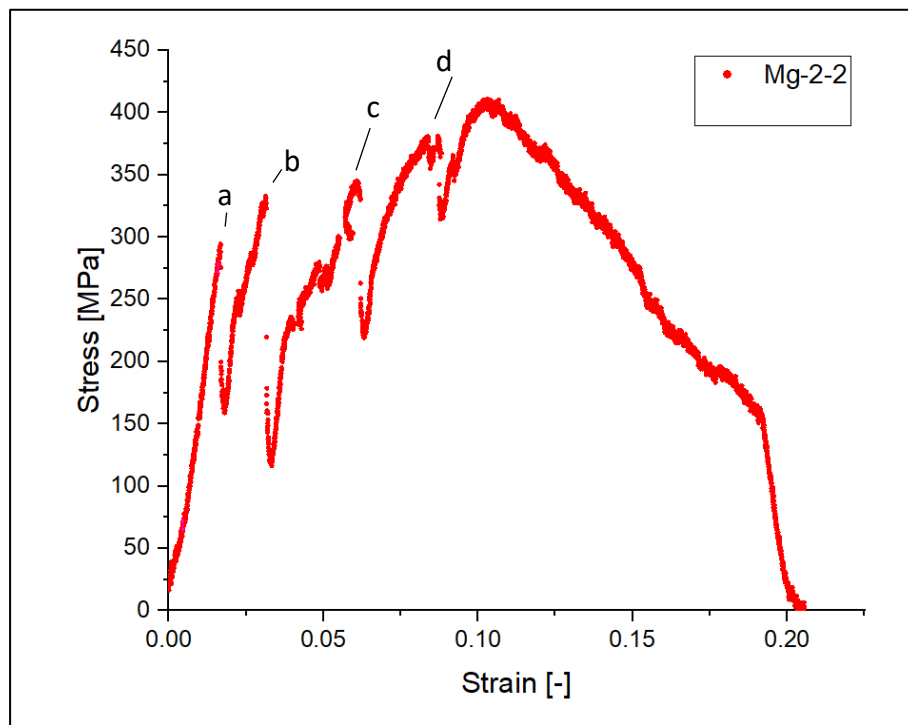
Figure 32: Stress-strain curve of Mg-2-2

The first stress drop of about $150\ MPa$ is clearly visible at a strain of $0.017\ (a)$. Until this point the stress rises linearly. After the drop the first crack becomes visible as the stress rises again. At the next stress drop of about $250\ MPa$ at $0.035\ (b)$, the formation of a second surface crack can be observed. Afterwards, the stress increases again, and small cracks continue to appear at $0.06\ (c)$. From an elongation of approximately $0.08\ (d)$ the main part of the elongation happens in the region of the second crack, which widens up to an elongation of 0.1, in conjunction with pronounced necking. Due to the large expansion of the crack, the sample becomes unstable, and the engineering stress continuously decreases. This sample behaves quite similarly to Mg-4-2, here too hardening can be seen, even more than in MG-4-2, but from 0.1 one of the cracks widens and the stress decreases.
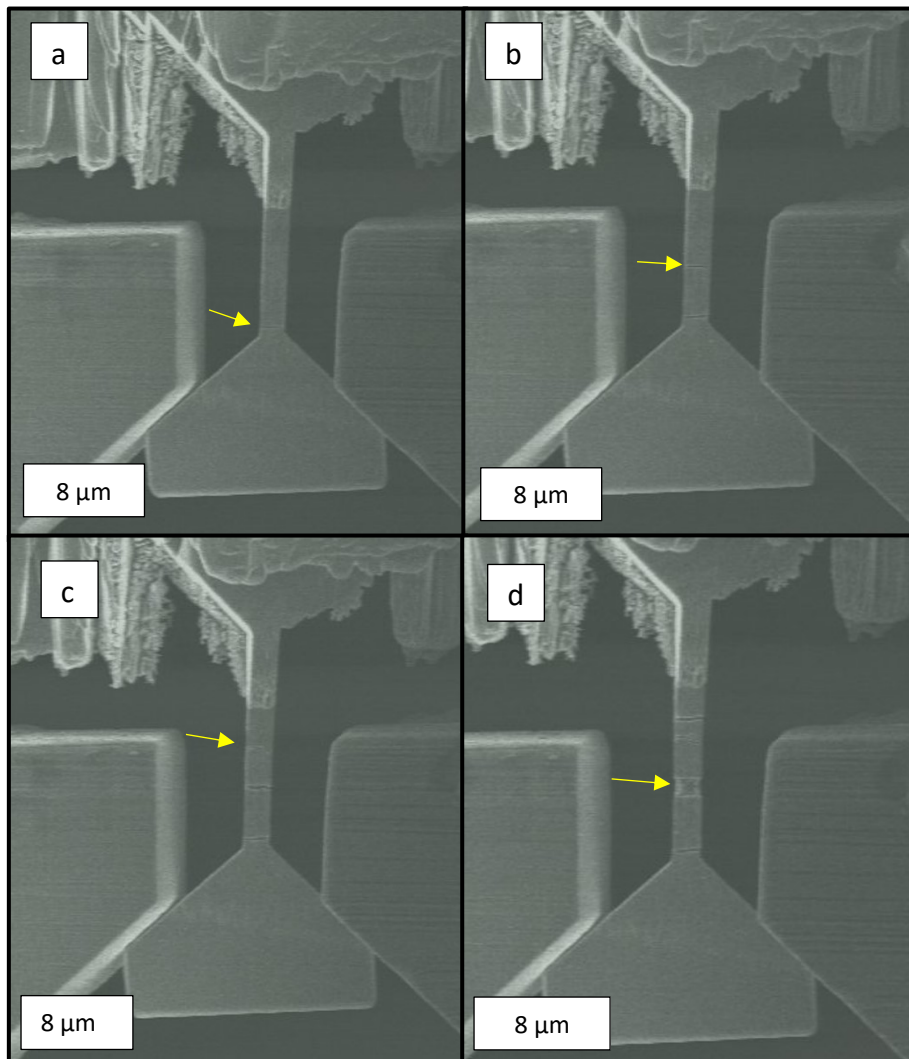
Figure 33:Images taken while testing Mg-2-2, the yellow arrows mark the cracks

Figure 33 shows the changes of the sample based on the in situ images taken during the test. The plastic deformation was 17% for Mg-2-1 and 18% for Mg-2-2. The maximum stress of Mg-2-2 is 70 MPa higher, although it should be noted that the area of Mg-2-2 is $4.4\ \mu m^2$ and that of Mg-2-1 is $5.5\ \mu m^2$. When comparing the appearance of the two samples after the test, it is noticeable that in Mg-2-2 the previously mentioned steps have formed over the entire width of the bar, which are also all perpendicular to the loading direction. In Mg-2-1, few of these steps can be seen, but there is also a slope on the surface of the specimen which has an angle of about 30° between the gauge part and the slip, depicted in Figure 34. It is possible that the imperfect geometry of the sample and the individual positioning of the gripper introduced bending stresses during the test. This could have caused the less ductile oxide layer to slip off and the pure Mg behind it to remain undeformed.
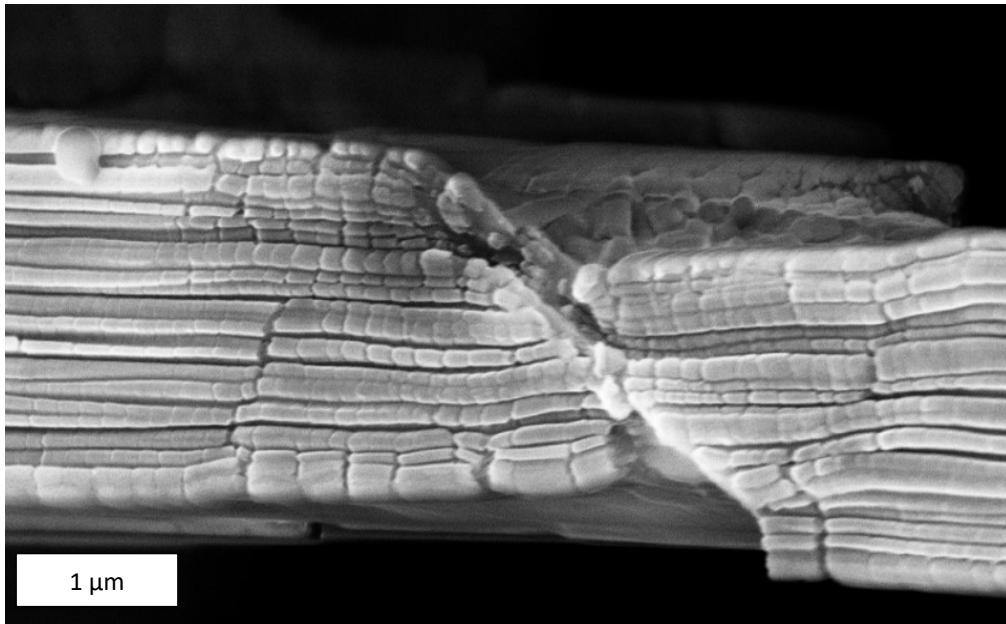
Figure 34: Close-up view of Mg-2-1

In Figure 35 the stress-strain curves of Mg-2-1 and Mg-2-2 are compared. The maximum stress for both happens at a strain of about 0.1. By expanding a step in sample Mg-2-2, the sample becomes unstable and the stress decreases. At this strain (Figure 33d) it is clearly visible that a surface layer (oxide layer) is cracking and that there is other material underneath, i.e. the pure Mg.
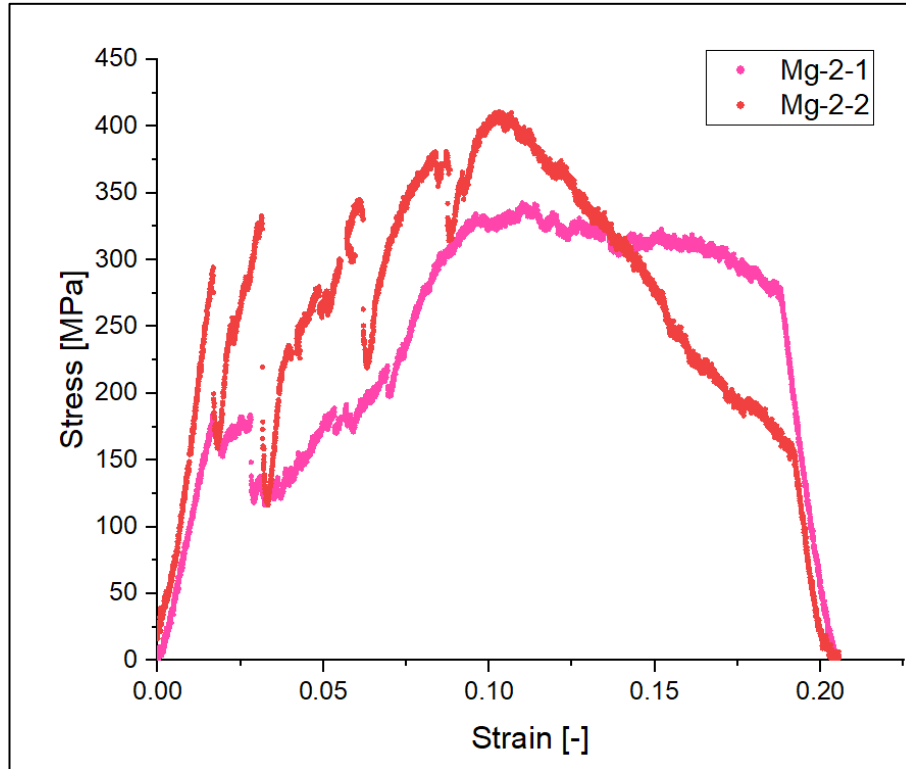
Figure 35: Comparison of Mg-2-1 and Mg-2-2

For Mg-2-1, the stress remains on a plateau and only decreases when unloading takes place. This plateau could indicate that one of the two pyramidal slip systems is activated, making it easier for the sample to deform. The CRSS for pyramidal $< c + a > \pi 1$ slip is around $133\ MPa$ and for $\pi 2$ $150\ MPa$. The plateau occurs at a strain of 0.1, so the sample is already deformed and it is difficult to assign the activated systems, because of the possibility that other slip systems could have been activated by previous deformation and formation of twins. However, the current values fit the CRSS values presented by Kiener *et al.* [1] for pyramidal slip $< c + a > \ \pi 1\ and\ \pi 2$.

4.2. Tensile tests of the Zn samples

In the case of Zn, the single crystallinity was guaranteed by a preceding EBSD-measurement. The orientation of the sample to the loading direction could also be implemented as planned. In contrast to Mg, only minor changes in the sample geometry were observed during testing, and no cracks or other significant damage were formed on the surface of the samples. Unfortunately, the head of some of the samples deformed considerably, which in turn introduces considerable experimental uncertainty.

Similar to the Mg samples, a size-effect can also be identified in these experiments, with the smallest ones exhibiting the highest strength, while the largest samples show the lowest strength, as depicted in Figure 36. What is striking at first glance in this overview is the stress drop of the samples Zn-4-1, Zn-4-2 and Zn-2-1, which all occur at similar strains. Sample Zn-2-1 also shows a much higher increase in stress than the other samples. The Zn specimens exhibit far less pronounced stress drops than the Mg samples, which in turn matches the images taken of the Zn samples, as hardly any abrupt changes can be seen. Instead, all samples show a pronounced flow plateau after the peak yield stress.
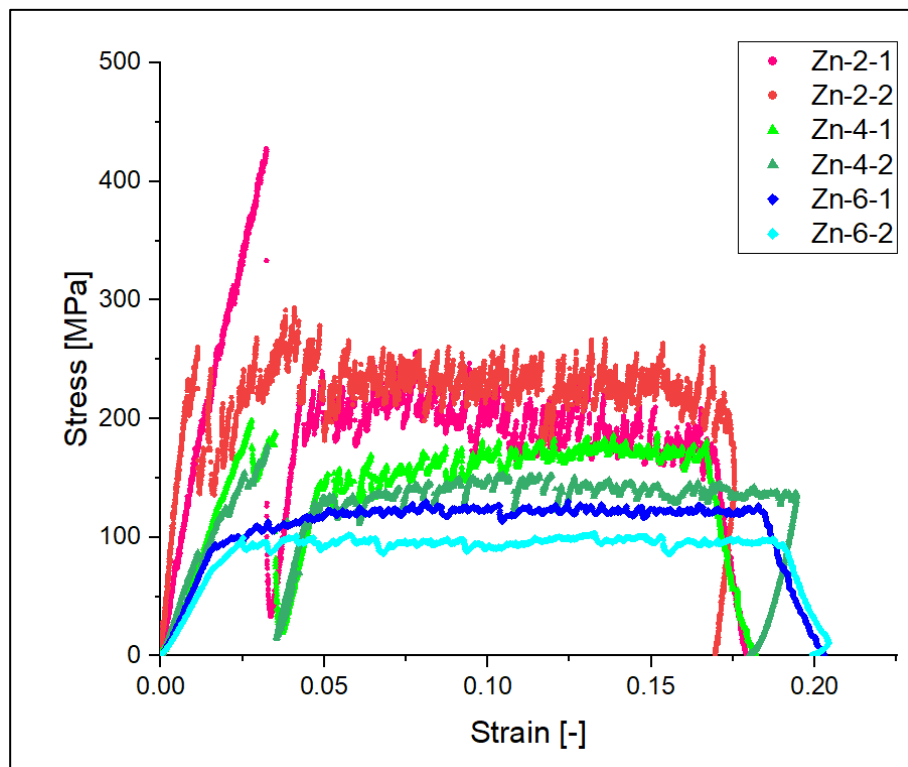
Figure 36: All stress-strain curves of the Zn samples

Due to the pronounced flow plateaus, it is likely that a slip system was addressed which withstands the deformation, such as the pyramidal $< c + a > \pi1$ and $\pi2$ systems. So none of the samples show any damage, only deformations, with respect to the plastic loading.

It cannot be fully explained why the head of some samples deformed so much, as the geometry of the samples before testing is almost identical. The strong deformation of Zn-4-2 can be seen in Figure 37 comparison to the undeformed head of Zn-4-1.

10 µm
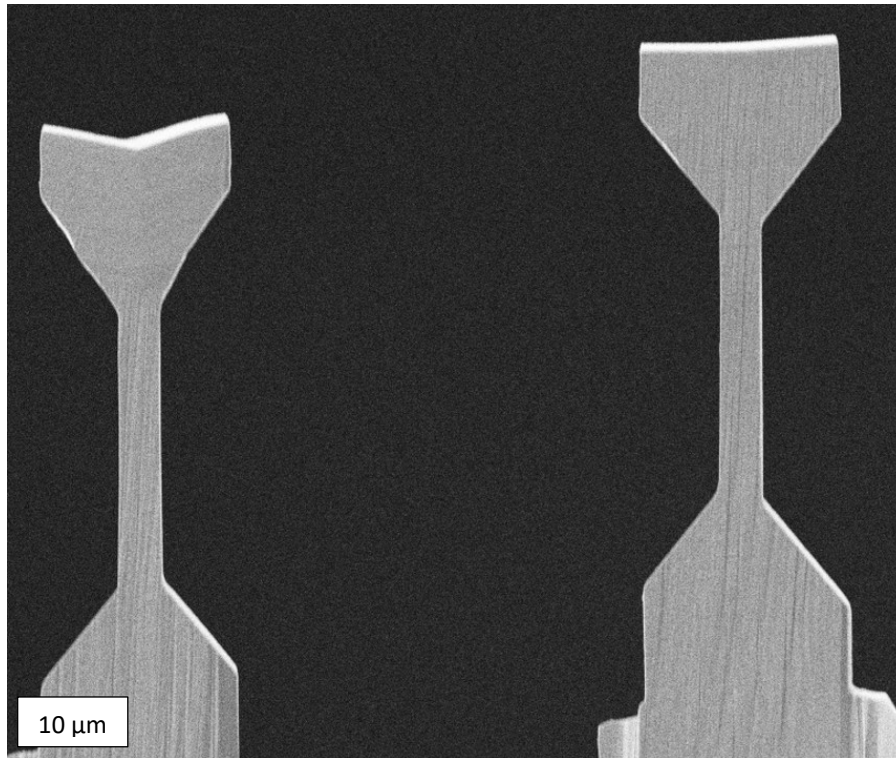
Figure 37: Comparison of Zn-4-1 and Zn-4-2 after the experiment, the head of Zn-4-2(on the left) is deformed

Since the crystal was again loaded along the c-axis, the basal $< a >$ and prismatic $< a >$ slip systems cannot be activated, only the pyramidal $< c + a >$ ones. For these two systems the Schmid factors m were calculated to evaluate the CRSS, via Schmid's Law (Equation 2). In two specimens, the formation of a twin could be observed, but not in the gauge part, but in the head of the specimen due to the loading of the gripper and following deformation. A CRSS can also be calculated for these twins.

To get the m values, the two angles, ϕ and λ, must be calculated [9]. For the pyramidal slip system $< c + a > \pi1$ $m = 0.3831$ was calculated and for the pyramidal slip system $< c + a > \pi2$ $m = 0.417$. The angles were calculated by marking the plane and direction in the unit cell using geometric considerations.

Tensile tests of the Zn samples

Figure 38 schematically shows the angle between the loading direction and the slip plane. Exemplary calculation for pyramidal slip $< c + a > \pi1$:

$$\theta = \arctan \frac{a}{c} = 25.01°$$

$$\lambda = 180° - 90° - 25.01° = 64.99°$$

$$m = \cos(\theta)\cos(\lambda) = 0.3831$$
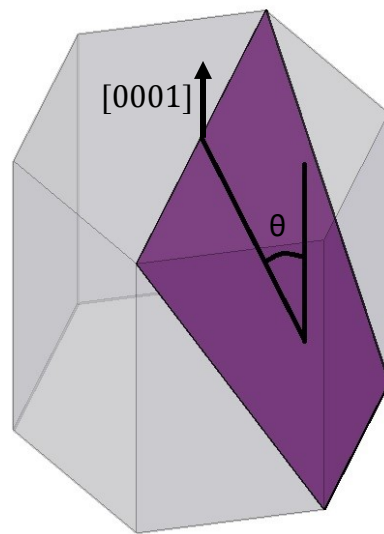
Figure 38: Angle between the loading direction and the slip plane

With these values, the CRSS can be calculated. Therefore, the stress at which the flow plateau begins was taken, as this is the stress necessary to activate the system. For Zn-2-2, Zn-6-1 and Zn-6-2 this stress corresponds to the yield stress.

Tensile tests of the Zn samples

In Table 5 some mechanical properties of the Zn samples are listed.

	Zn-6-1	Zn-6-2	Zn-4-1	Zn-4-2	Zn-4-1	Zn-4-2
max.stress [MPa]	130	103	198	177	198	177
App. elastic modulus [GPa]	6.25	4.87	12.97	10.12	12.97	10.12
yield stress [MPa]	92± 1.6	93± 3.4	189± 8.5	169± 8.8	189± 8.5	169± 8.8
flow plateu [MPa]	119± 17.0	96± 3.3	163± 12.2	137± 7.6	163± 12.2	137± 7.6
CRSS $\pi 1$ [MPa]	38± 0.7	39± 1.4	68± 5.1	57± 3.2	68± 5.1	57± 3.2
CRSS $\pi 2$ [MPa]	35± 0.6	37± 1.3	62± 4.7	52± 2.9	62± 4.7	52± 2.9

Table 5: Material properties of Zn samples

4.2.1. Results from Zn-6

In **Fehler! Verweisquelle konnte nicht gefunden werden.** the stress-strain curve of the sample Zn-6-1 can be seen. The transition from the elastic to the plastic range takes place at a strain of 0.016 (a) and a stress of about 94 MPa. From this point the stress increases until a plateau forms at an elongation of 0.05, with a stress of 119 MPa.
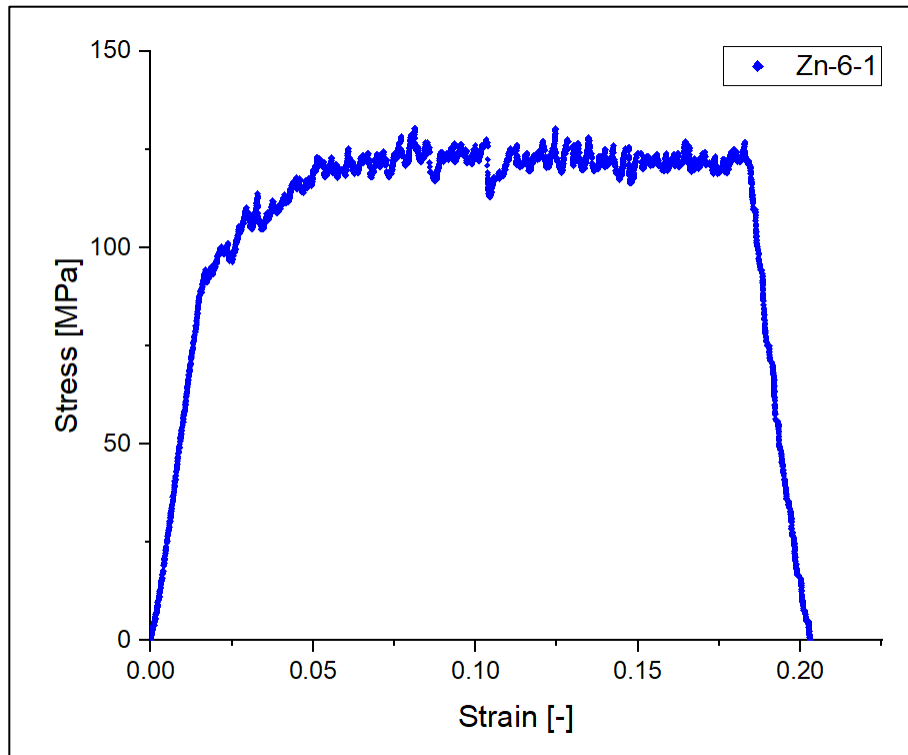
Figure 39: Stress-strain curve of Zn-6-1

The interval in which the stress varies is about 17 MPa, which again is rather small compared to Mg. No surface damage on the sample can be observed.
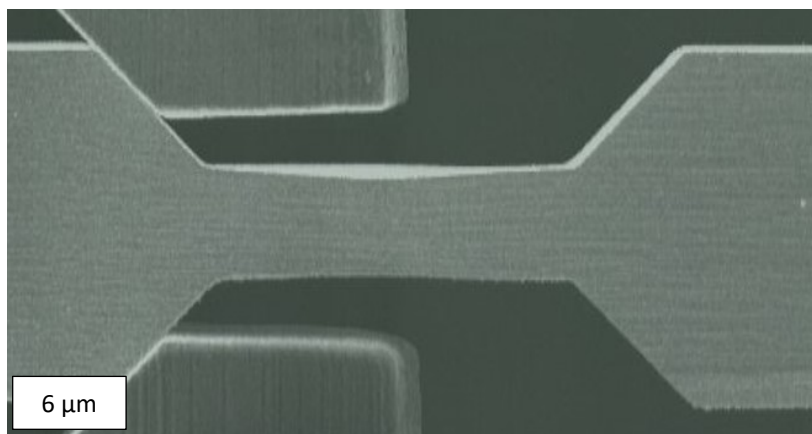
Figure 40: In situ image of Zn-6-1

The stress drop of 14 MPa at 0.104 strain can be attributed to a start of the slight necking of the sample, shown in the *in situ* image in Figure 40.

When comparing the two stress-strain curves of Zn-6-1 and Zn-6-2, shown in Figure 41, they show similar slopes in the linear elastic range, whereby for Zn-6-2 the slope decreases slightly at 75 MPa, while for Zn-6-1 the slope decreases at 90 MPa. For both, the transition from the plastic to the elastic range is observed at a strain of 0.015.

Unfortunately the deformation of Zn-6-2 occurred mainly in the head, as the measurement of the bar before and after testing shows only an elongation of 1.2%, whereas in Zn-6-1 a lengthening of 17.9% occurred. A difference between the plateaus of up to 30 MPa can be observed.
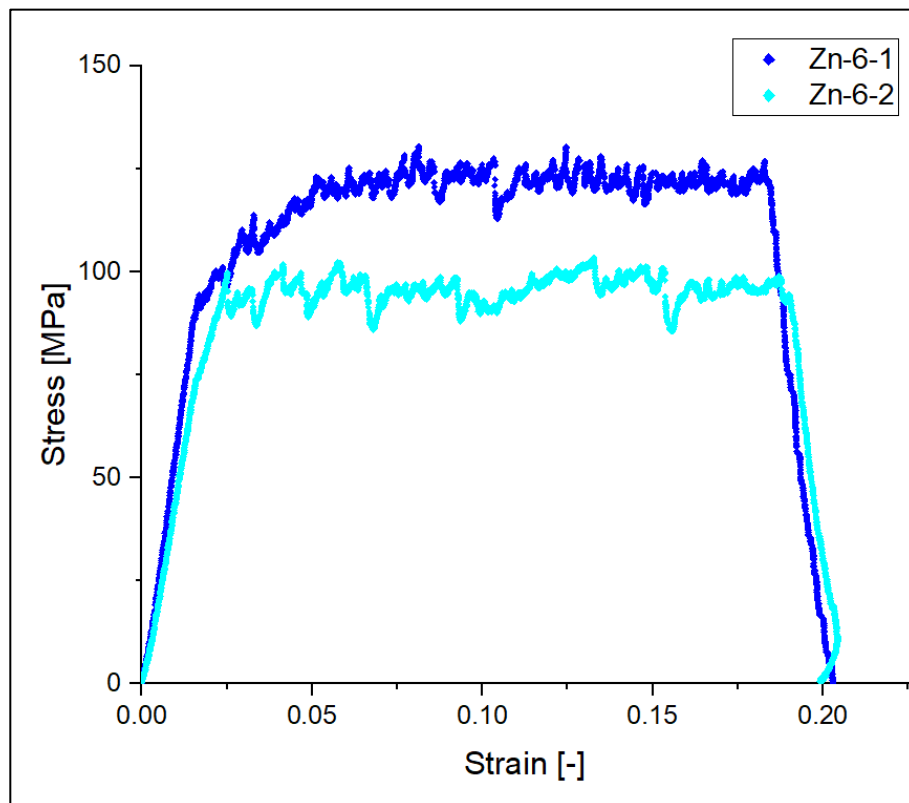
Figure 41: Comparison of Mg-6-1 and Mg-6-2

In Zn-6-2, the head of the sample has deformed strongly, as a result a twin has formed, depicted in the EBSD-Scan in Figure 41. It is important to mention, that the twin did not form because of the intended pulling on the sample, but through the bending stresses caused by the gripper. The EBSD scan of Zn-4-2 strongly resembles that of Zn-6-2, the same deformation has occurred in the head of the samples.

Results from Zn-6

As can be seen in Figure 6 [4], for this load there should only be the possibility that a tension twin, namely $(11\bar{2}1)\,[\bar{1}\bar{1}26]$, has formed, this was accordingly recalculated since the tilt between the initial unit cell and the twinned unit cell is known from the measurement in the EBSD.

The angle between the initial unit cell and the twin is 13° each, thus resulting in an angle of 26° between the two twins, the calculation with the EBSD has an uncertainty of 2°. To prove this angle for the proposed tension twin, the angle between the plane and the loading direction was calculated using trigonometry, resulting in an angle of 15°. With the uncertainty of the EBSD measurement, which could explain the 2° difference, and the calculation of the angle, it can be claimed that the $(11\bar{2}1)\,[\bar{1}\bar{1}26]$ tension twin has formed. The same tension twin has formed in Zn-4-2.

$$\tan\theta = \frac{h}{c} \quad h = a * \cos\left(\frac{\pi}{3}\right)$$

$$\theta = arctan\left(\frac{h}{c}\right) \approx 15°$$
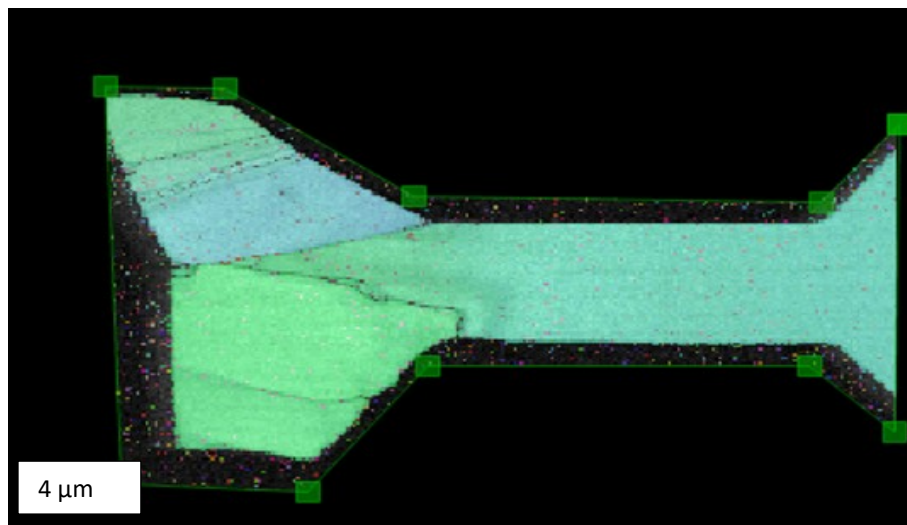
Figure 42: EBSD-scan of Zn-6-2

h was defined as the distance from the point of penetration of the [0001] direction through the unit cell to the bottom edge of the plane and $c = 0.4946\,nm$ is the lattice parameter.

The EBSD measurement in Figure 42 shows the deformation caused by the gripper. In the head of the sample, the twin boundary can be seen between the differently oriented areas in the crystal.

4.2.2. Results from Zn-4

The stress initially increases linearly for Zn-4-2, which can be seen in Figure 43 with small $(5 - 15 \, MPa)$ stress drops and reaches the highest stress of $177 \, MPa$, which is then followed by a large stress drop. This drop of $160 \, MPa$ occurs at a strain of 0.035 and can be attributed to a sudden extension, which is noticed in the images taken.
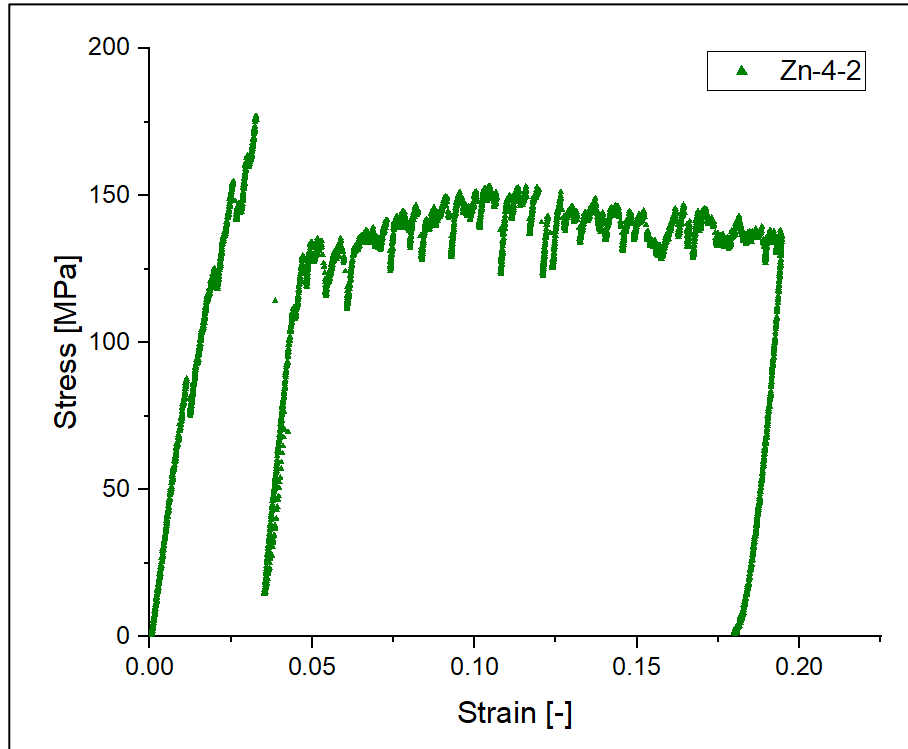
Figure 43: Stress-strain curve of Zn-4-2

After the stress drop, the stress rises to a plateau, at values between $120 \, and \, 150 \, MPa$. The images taken during the experiment do not show any sudden changes, but a uniform deformation in length. In this sample the head has deformed strongly, in the other sample with the same dimensions this did not happen. No difference indicating this is visible comparing the two curves.

When analyzing the EBSD data of Zn-4-1, it was found that the sample is also single crystalline after testing and no twins have formed. A slight change in orientation, labelled as (a) in Figure 44, has taken place in the passage from the gauge section to the head. Since the orientation differences are small, it is rather unlikely that a twin has formed.
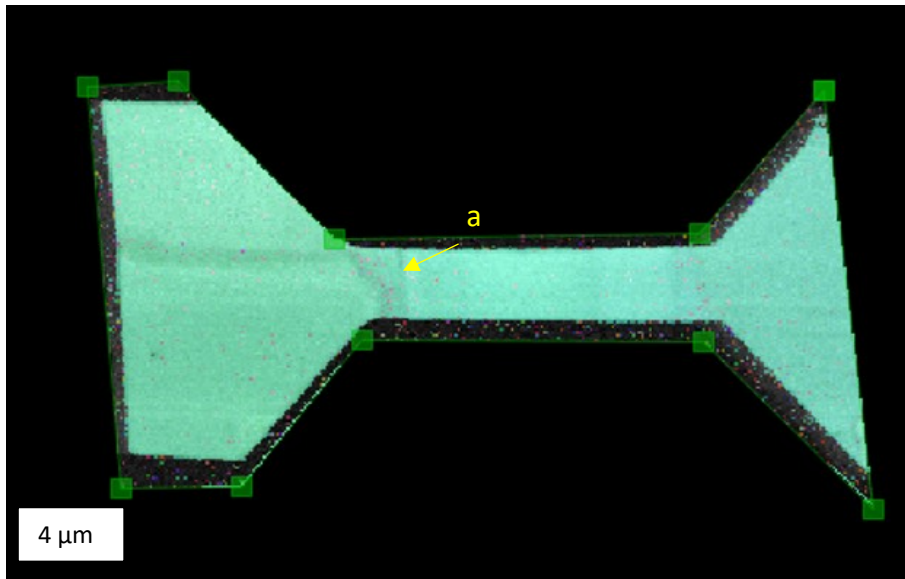
Figure 45: EBSD-scan of sample Zn-4-1

The previously determined tension twin can also be seen in Figure 45, the EBSD-scan of Zn-4-2. In the scan, a defined boundary between two differently oriented areas is evident, suggesting the formation of a twin. The supposed twin boundary (a) is again marked with a yellow arrow. It should be remembered here that the twin was not formed by pulling on the sample, but due to bending stresses exerted by the gripper. As previously elaborated for Zn-6-2, the $(11\bar{2}1)\ [\bar{1}\bar{1}26]$ tension twin has also formed here.
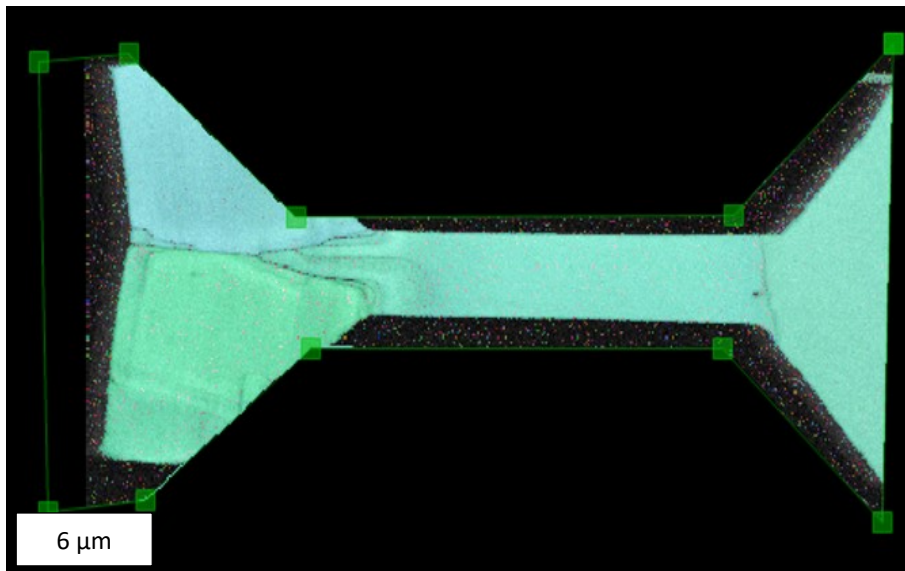
Figure 44: EBSD-scan of sample Zn-4-2

During comparison of the two stress-strain curves, Figure 46, no evident differences can be observed. Both samples show a massive stress drop at 0.035 strain after reaching the highest stress, which is $200\ MPa$ for Zn-4-1 and $175\ MPa$ for Zn-4-2, respectively.

When measuring the gauge-length before and after the test, an extension of 11.9% could be measured, while for Zn-4-2 this extension is only 5.8% because the deformation mainly took place in the head of the sample. In both samples there is a sudden elongation of the specimen related to the stress drop. It was initially assumed that twins formed along the gauge part, but this could be disproven by the EBSD-measurement. After the massive stress drops, the stress increases and reaches a plateau, with a difference up to 30 MPa between the samples.
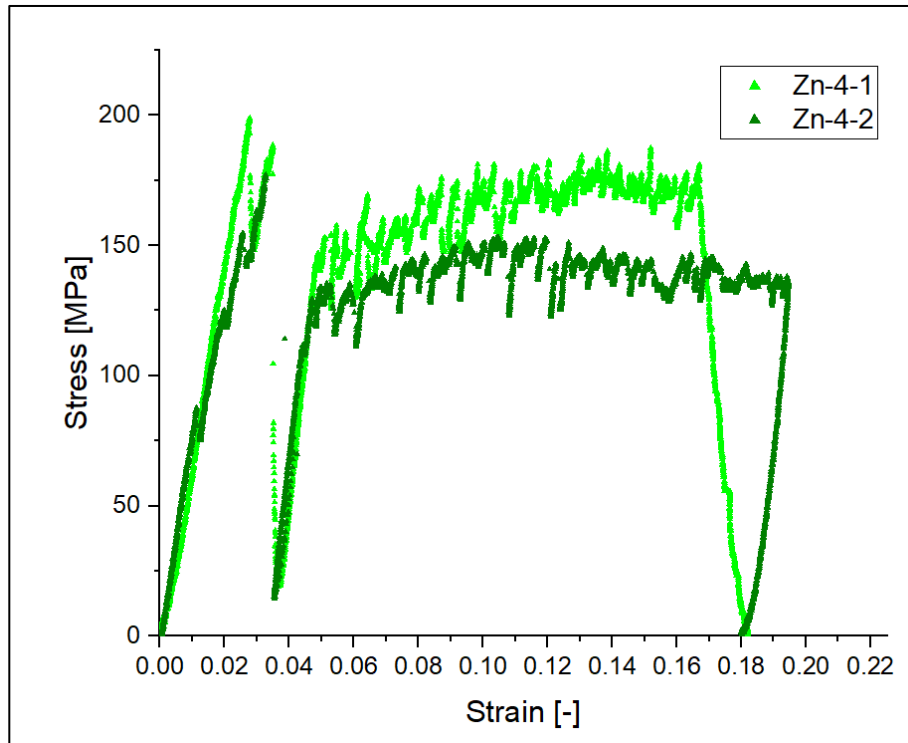
Figure 46: Comparison of Zn-4-1 and Zn-4-2

4.2.3. Results from Zn-2

This sample seems to be particularly interesting because the stress rises many times higher than in other tested samples, as can be seen in Figure 47. The value of the maximum stress is $427\ MPa$, whereas the sample Zn-2-2 only reaches a maximum stress of $293\ MPa$, although the latter has slightly smaller dimensions.
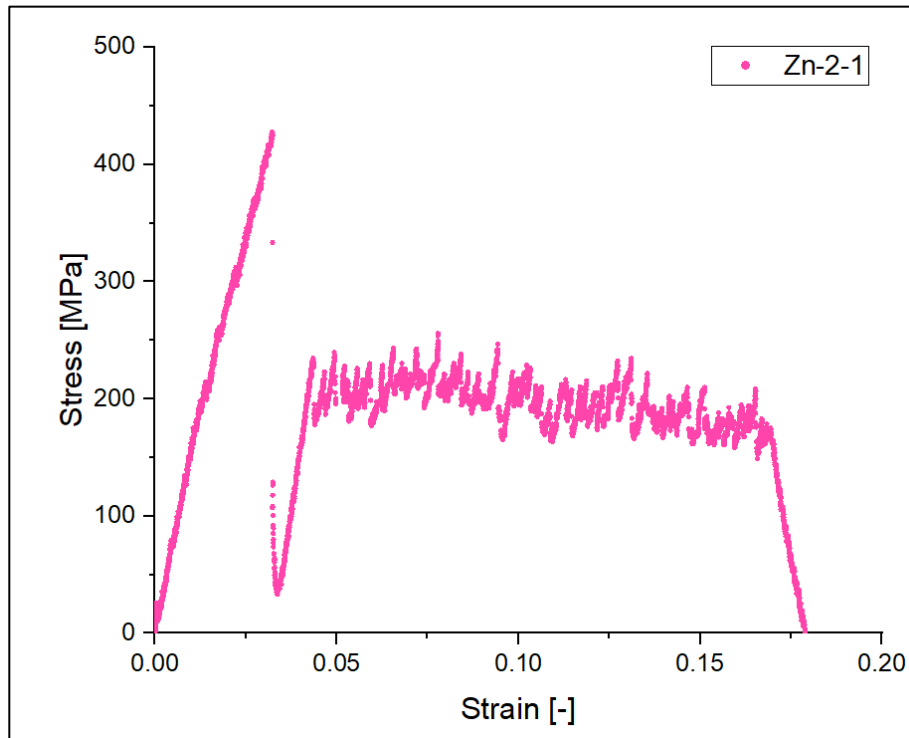
Figure 47: Stress-strain curve of the sample Zn-2-1

As with the other samples, an abrupt elongation of the sample can be observed, which again is related to the massive stress drop at a strain of $0.035\ (a)$. After the massive drop, the stress rises to a plateau of about $175\ to\ 250\ MPa$. The stress drops that occur along this plateau cannot be assigned to any noticeable event during the experiment.

Figure 48a shows the sample before testing and Figure 48b after testing. There is hardly any necking recognizable. It rather appears as if the entire gauge length has lengthened evenly.
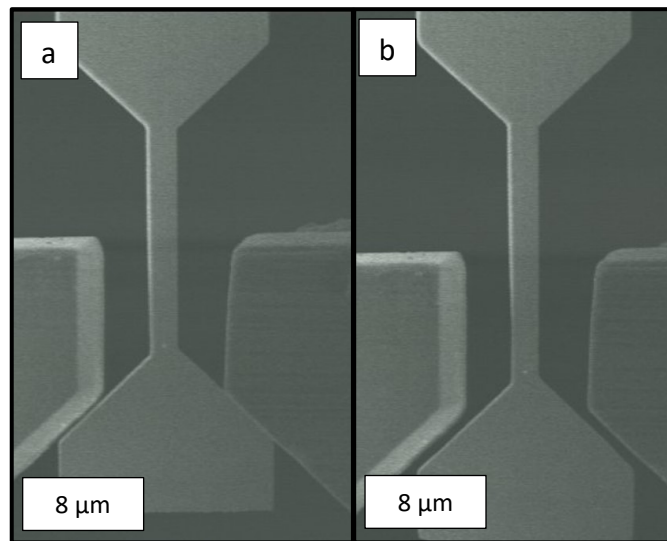
Figure 48: Zn-2-1 before(a) and after (b) testing

For the two samples Zn-2-1 and Zn-2-2 no deformation of the head and no twinning could be evidenced. At the gauge of Zn-2-2, a constriction can be noticed., In Figure 49 the misorientation of this area can be seen, the maximum angle is about 3.5° for the deformation in the gauge section. The misorientation that appears on the underside of the head of the specimen could be an instability in the evaluation or deformation from where the gripper contacted the specimen.
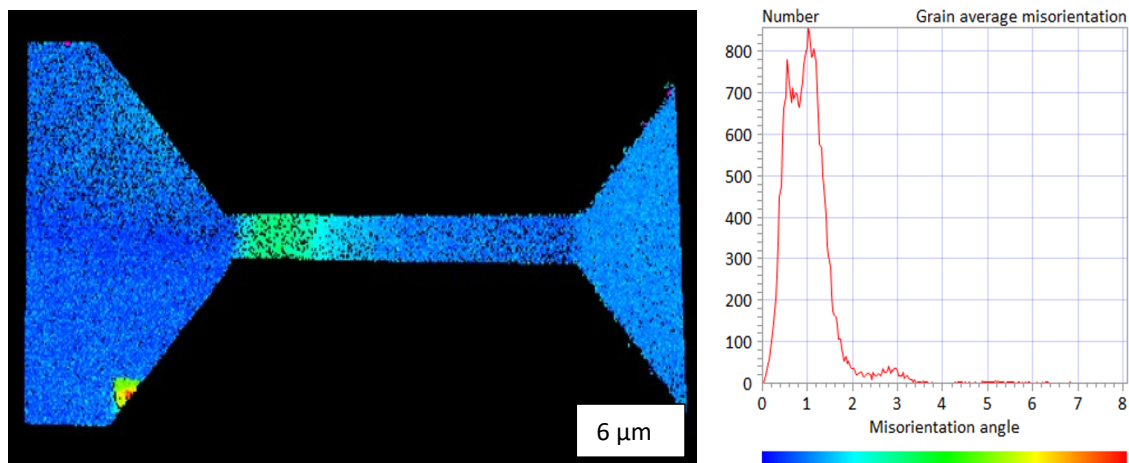
Figure 49: Misorientation average and histogram of Zn-2-1

Therefore, no change to a distinctly different orientation took place, suggesting a pure accumulation of dislocation plasticity in both samples.

Results from Zn-2

The misorientation for Zn-2-2, depicted in Figure 50, may have been caused by sliding, and this sliding may have caused a kink band. The maximum angle of misorientation is between 0.5 and 1° and appears on the underside of the head of the specimen could be an instability in the evaluation or deformation from where the gripper contacted the specimen.
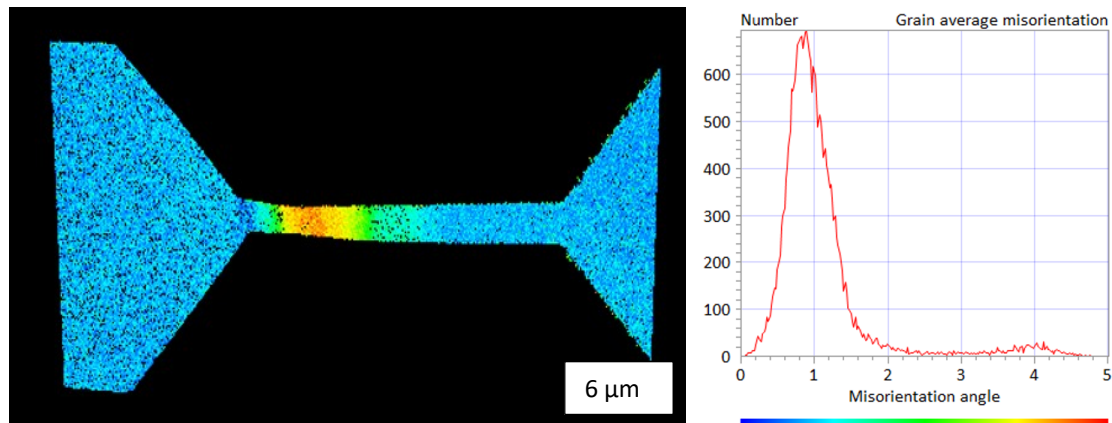
Figure 50: Misorientation and histogram of Zn-2-2

When comparing the two stress-strain curves in Figure 51 a massive drop in stress at 0.035 strain of Zn-2-1 is noticeable, which occurs in the same range as for Zn-4-1 and Zn-4- 2.
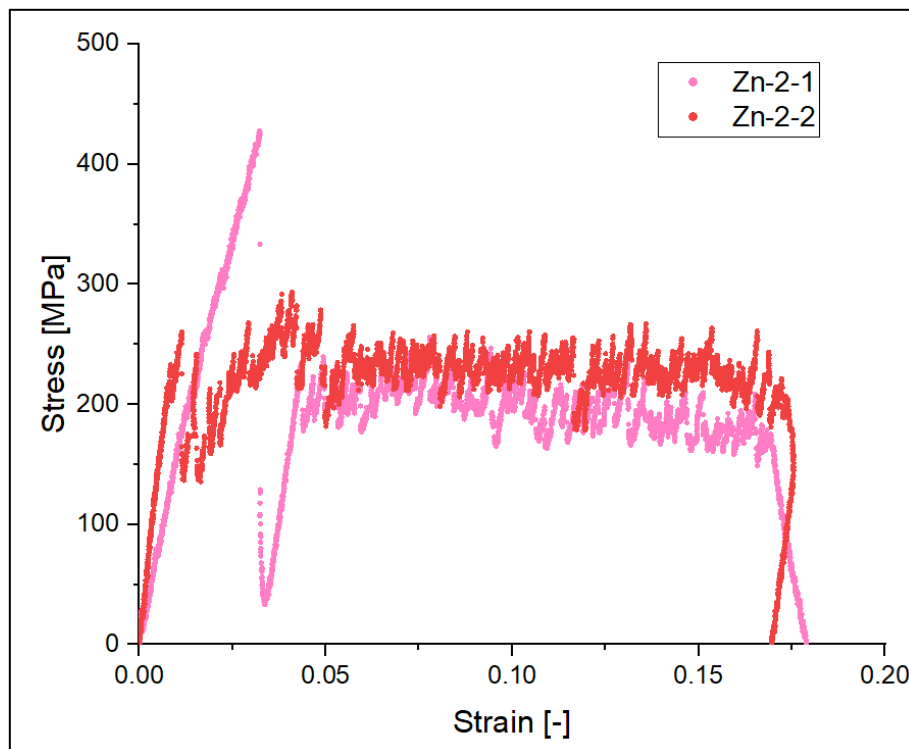
Figure 51: Comparison of the stress-strain curves of Zn-2-1 and Zn-2-2

Results from Zn-2

It is also interesting to note that the stress rises to $428\ MPa$ before dropping to $37\ MPa$. The maximum stress is many times higher than in any other sample, and $140\ MPa$ higher than Zn-2-2. A sudden elongation of the sample could also be observed here, again without the formation of a twin.

5. Size effect and analysis of the possible deformation behaviour

Micromechanical experiments are challenging, and there is certainly a steep learning curve involved when conducting such experiments for the first time. In retrospect, when dealing with the experimental set-up and the execution, some factors could be improved in order to get more reliable values. For example, the choice of the gripper was not optimal, because it was too wide and therefore the whole contact area of the specimens heads could not be used, which resulted in the introduction of bending stresses and the deformation of some specimen heads. This should be avoided as the force was not precisely focused on the gauge part. As a result, the data can potentially be misinterpreted with regard to the size effect, and also the comparison between the individual specimens remains rather challenging, since the deformation did not take place in the gauge part for all of them as intended.

5.1. Deformation behaviour of Mg

Due to the oxide layer forming on the magnesium samples, which is approximately $150 - 200nm$ thick, it was not possible to make accurate EBSD measurements for the individual specimens and therefore only an estimate on potential occurring, deformation mechanisms, is given. If these experiments were to be repeated, it would be advantageous to perform the *in situ* tensile test immediately after the final polishing of the samples.

However, as mentioned in the results, it can be assumed that upon loading along the c-axis of the crystal only a tension twin or the two pyramidal $< c + a >$ slip systems can be activated. The many pop ins along the stress-strain curves and also the deformation of the sample heads, like in Mg-4-1, could be indications for the formation of a tension twin as in the deformed Zn heads. The tension twin is defined by the $^{c}/_{a}$-ratio and therefore not the same tension twin as in Zn, depicted in Figure 6 [4]. The two possible tension twins are namely $\{10\bar{1}1\} < 10\bar{1}2 >$ and $\{10\bar{1}3\} < 30\bar{3}2 >$ [4].

As mentioned in the results, a sudden elongation can be observed during the tensile test of sample Mg-6-1. Perhaps only in this sample a twin was formed, as the required stress for the formation of a twin increases the smaller the sample diameter is and due to the non-optimal loading of the gripper.

The deformation in Mg-6-2 was made more difficult to interpret due to the slipping of the head. But again, it would be important to be able to assess the surface precisely to identify the formation of a twin, which is likely to be prevented by the oxide layer.

Another possibility to explain the pronounced stress drops, which does not exclude twinning, is the tearing of the oxide layer. It can be assumed that the layer is not sc and behaves much less ductile than the high purity magnesium. The rupturing of the layer, which can be observed in the images taken during the experiment, can cause the material underneath to tear along with it, as can be seen in samples Mg-4-1 and Mg-2-2. Thus, the deformation behaviour is strongly influenced by the oxide layer; without it, the samples should behave more ductile and show a more uniform behaviour, i.e. fewer stress drops and less strain hardening.
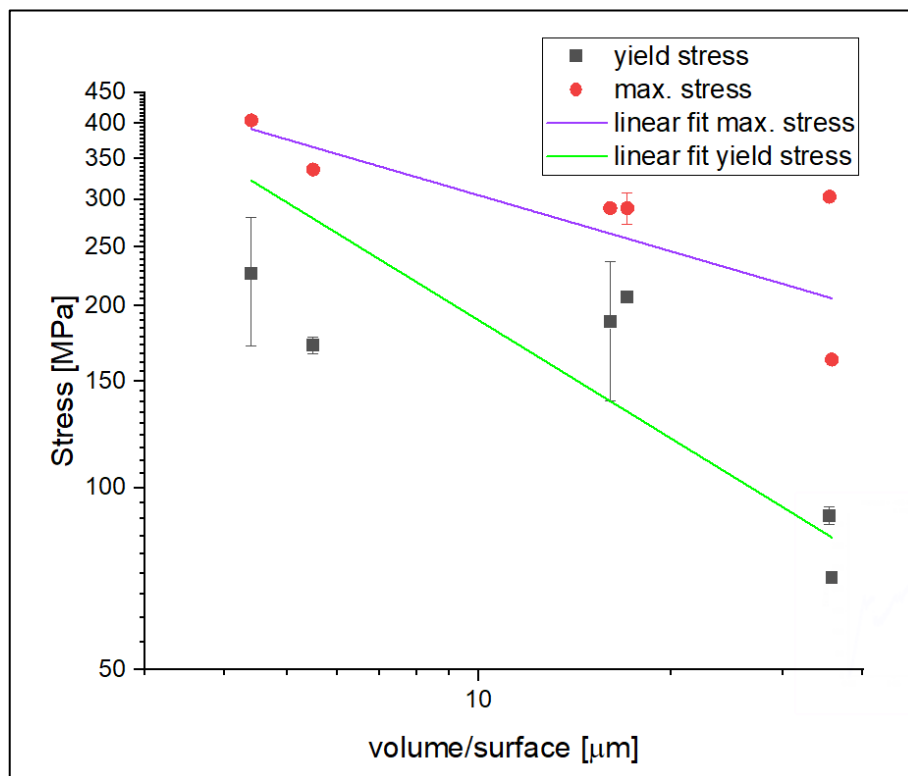
Figure 52: Representation of the max. stress and yield stress as a function of volume-to-surface-ratio

Due to these influences, i.e. the oxide layer, the unintended twinning of the lamella before the experiment and also due to the partly asymmetrical geometry, the values are more scattered than those of the Zn samples and it is more difficult to establish a relationship between sample size and strength.

In Figure 52 the max. stress and yield stress were plotted as a function of the volume-to-surface-ratio in a double logarithmic scale, where a linear fit can be drawn for both stress values, respectively. As there is significant deviation from the exponential behavior, more data would be necessary to make a well-founded statement. Nevertheless, the slope of the linear regression for the yield stress is $m = -0.65$ and for the max. stress $m = -0.31$.

Horstemeyer [33] reported the relationship between the normalized resolved yield stress and volume-to- surface-area ratio for Ni with a slope of $m = -0.38$ for the linear regression of the data.

Through simulation, it can be concluded that plastic deformation is inhomogeneous and thus yield strength is dependent on sample size and is inversely proportional to the ratio of sample size to volume [33].

It is not clear if higher strengths associate with higher deformation gradients or with low dislocation conditions [2], [33]. This trend can also be observed in the data obtained in the experiments and thus shows reasonable agreement, although the experimental conditions were not ideal. The slope of the linear regression for the yield stress is $m = -0.65$. This value is higher than that for the fcc Ni data, but it must be considered that Horstemeyer *et al.* [33] plotted the data different, as previously described, the normalized resolved yield stress is used. The slopes could be expected to differ because in the Mg experiments the area was up to about $36 \ \mu m^2$, which is much larger than the samples studied here, thus the size effect could be more pronounced because of the big differences in size.

By introducing dislocations through deformation, for example, the size effect can be superimposed [21]. This could also have an influence here, since, as mentioned, the sc condition is not guaranteed and dislocations might have been introduced during preparation. However, this should have less influence since a correlation between size and yield stress could be found.

Dou *et al*. [3] have developed a universal scaling law that links yield stress to sample size, with relation to the Burger`s vector and the shear modulus. It is consistent with the other studies, showing an increase in stress with a decrease in sample diameter. The law was developed for fcc materials and was also reported applicable to Mo and Mo alloys, although Mo is bcc.

In the law, the slope of the linear regression in the logarithmic correlation between stress and pillar diameter enters as an exponent. For fcc, this exponent is $m = -0.66$ [3].

For better comparability, the yield stress and max. stress of Mg were plotted against the gauge width in Figure 53, resulting in a slope of $m = -1.05$ for the yield stress and $m = -0.72$ for the max. stress. Like in the previous comparison, the values of Mg are higher, although in this case it is even more difficult to find a linear relationship. The scaling should apply if $d/b < 10^3$, where b is the Burger`s vector and d is the diameter of the specimen. This cannot be guaranteed for the investigated sizes.

Dou *et al.* [3] state that the strengthening mechanisms depend on the interactions of the dislocations and the dislocation line stress. The dislocation line stress depends on the elastic modulus and the Burger`s vector and represents the operating stress of an isolated single-arm dislocation source without lattice resistance. Thus, the scaling law becomes invalid when the Peierl`s stress, which depends among other things on the Burger`s vector, increases.

Since the Peierl's stress for hexagonal and fcc materials is smaller than the critical stress necessary for a dislocation to cut or pass other dislocations, a similar behaviour can be expected and thus the comparison with the Ni data seems valid. The determined exponent for Ni, Au and Al is $m = -0.66$.
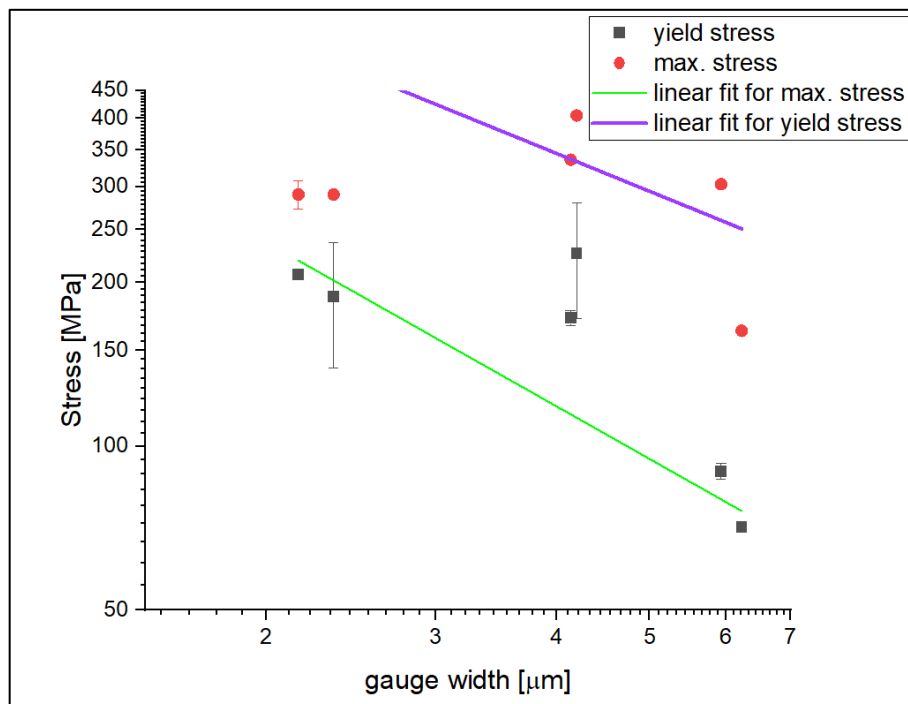
Figure 53: Representation of the max. stress and yield stress as a function of the gauge width

The Peierl's stress for bcc materials is higher than the fracture stress and thus the law can be expected not to apply as well to bcc Mo, and even less so to metals with even higher Peierl's stress [3], [5].

Abad et al. [34] report that the exponent for fcc metals is in the range of -0.6 to -1, and is lower for bcc metals as they do not show such a pronounced size effect. These different dependencies in terms of size are due to the influence of the lattice resistance on the plastic strength of the bcc metals. The lattice resistance is in turn dependent on the Peierl's potential, which is higher for bcc metals than for fcc. Due to the high Peierl`s potential in bcc metals, the screw dislocations are less mobile than edge dislocations. Thus, the decreasing mobility of the screw dislocations is proportional to the decreasing size dependence.

Greer *et al.* [21]suggest that due to the high Peierl`s barrier for non-basal slip and twinning in Mg, there should be more of a similarity to the behaviour of bcc materials. The normalised shear stress is applied over the sample diameter and an exponent $m = -0.44$ is determined for Mg. This value increases to $m = -0.66$ for cold worked Mg as there are more dislocations in the material. As it cannot be proven which deformation mechanism was activated in Mg and the determined exponents are up to twice higher, this statement cannot be supported with the data.

5.2. Deformation behaviour of Zn

To focus once again on the size effect, the flow stress and yield stress of the Zn samples are plotted against the gauge width on a double logarithmic scale in Figure 54. Here again the trend towards stress increase can be seen as the sample size decreases. The slope of the linear regression for yield stress is approximately $m = -1.25$ and for flow stress $m = -0.67$.
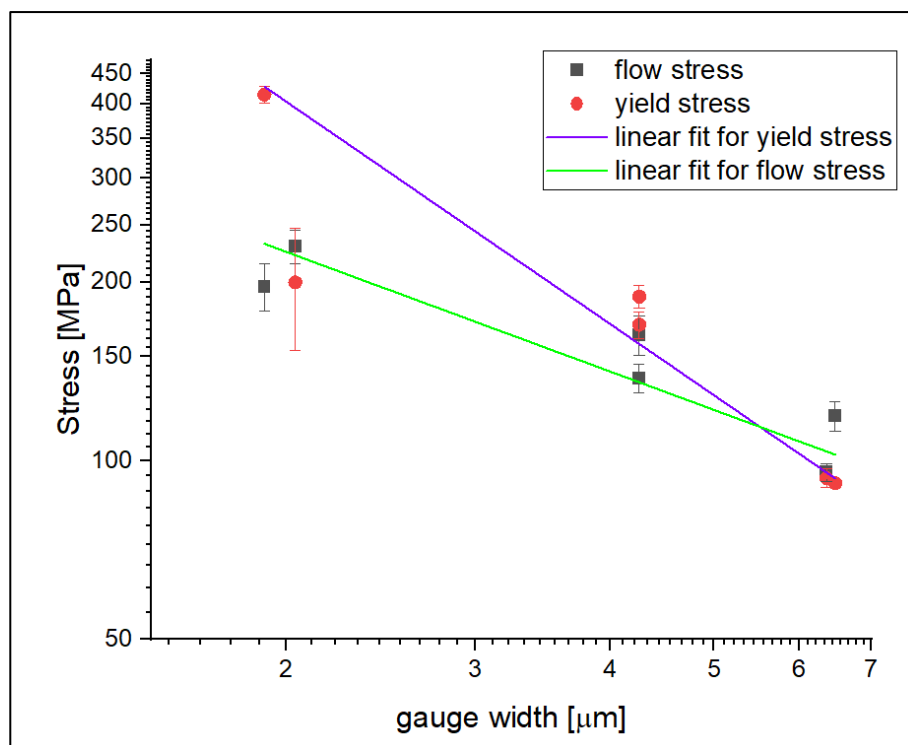
Figure 54: Representation of the flow stress and yield stress as a function of the gauge width

This linear relationship can only provide limited information due to the small number of samples, as there are outliers among the samples which can be taken into account or not. The linear trend is more consistent for the flow stress, here it should be mentioned that the stress for the samples with deformed heads is $30\ MPa$ lower, which is possibly caused by the bending load on the head.

As the Zn samples show these pronounced flow plateaus, it is possible to compare them with the results of the study from Greer *et al.* [21]. They distinguish between the intrinsic and extrinsic size effect. The intrinsic size effect relates to microstructure, grain and precipitate size, twin boundary spacing and the density of dislocations and affects materials of any

dimensionality. The extrinsic size effect refers to the sample size. The study compares the relationship between stress and sample size for different metals, including bcc, fcc and hcp sc. Mg as well as Ti and their alloys were compared, which were all tested under compression. It is claimed that for all fcc materials unified power-law slope is around -0.6, which is appropriate for the size dependence of the flow stress. Due to the high scatter of the yield stress, the evaluation of this slope is difficult, and the value of -1.25 seems exaggerated.

The exponent $m = -0.66$, which was determined by Dou et al. [3] for Ni, Au and Al, is almost the same as that for the flow stress of the Zn specimens. Due to the small number of data points, it must also be assumed here, although the values appear very valid, that the experimental difficulties have influenced the results.

As mentioned earlier, Abad et al. [34] find exponents between -0.6 and -1 for fcc metals, which is further evidence that the Zn specimens behave similarly to fcc materials.

5.3. Comparison of Mg and Zn

Figure 53 shows the CRSS for the two pyramidal $< c + a >$ slip systems for both materials. Since the CRSS depends on the determined stresses, the smaller dimensions also have a higher
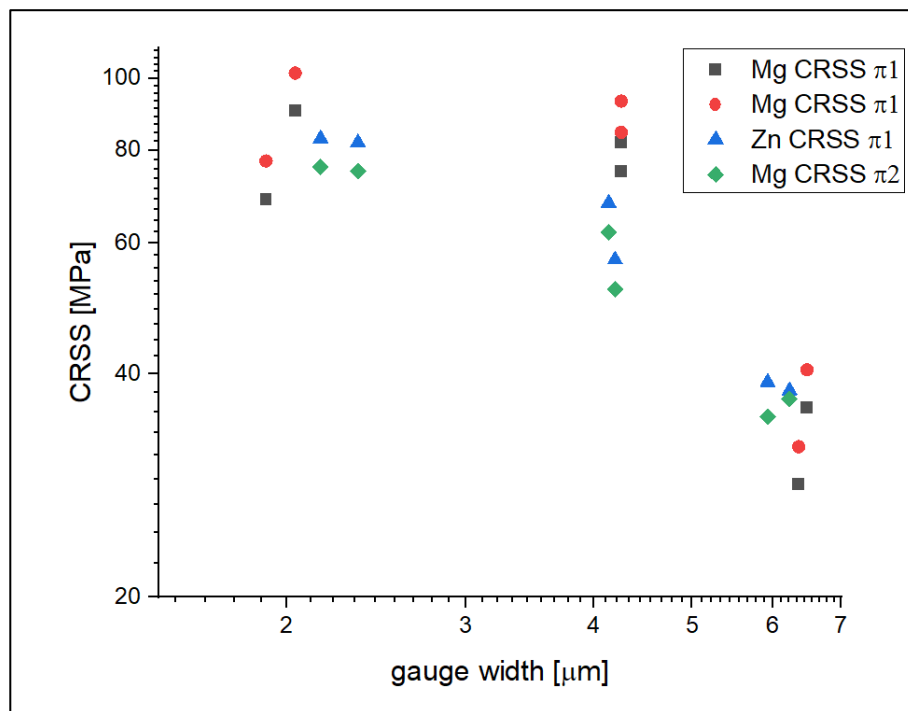
Figure 55: Represantation of the CRSS over the gauge width

The size dependence is more pronounced for the samples with a diameter smaller than or equal to $4\ \mu m$ [23]. Due to the large deviations and the previously described influences, no significant difference between the CRSS of Mg and Zn is evident. Yang *et al.* [9] shows CRSS for sc Zn and Mg, the CRSSs are hardly comparable with the experimentally determined, but one can compare the ratio between the materials. The CRSS for Zn is more than three times lower than for Mg, which cannot be supported, as can be seen in Figure 53. No linear relationship can be found for the correlation between CRSS and area on a logarithmic scale, which would again require more data points and better execution of the experiments so that the values are more consistent. It can be argued that especially the CRSS of Mg is strongly distorted by the influence of the oxide layer and therefore not well comparable with Zn. Further, the exact orientation of the Mg crystal would be necessary to be able to say for sure which slip systems and twins can be activated and the sc microstructure would have to be guaranteed.

6. Conclusion

During the execution of the experiments, some problems occurred which should be avoided in the future. As mentioned before, problems such as the deformation of the sample heads occurred due to the non-optimal choice of the gripper. One difficulty is the positioning of the gripper, as each sample is cut into the lamella individually, which can lead to the samples being slightly twisted or tilted. This can hardly be compensated by the gripper and therefore unintended bending stresses occur during the experiment. When using a smaller gripper, the risk of damaging a sample during positioning is increased, as there is much less room for maneuvers to position the sample correctly in the holder. Another important point when processing the samples in the FIB is to ensure that the surfaces are as smooth as possible. This was achieved well for the Zn samples, but not too well for the Mg specimens, mostly due to strong curtaining artefacts and redeposition during the fabrication process.

As described in the results, an oxide layer with a thickness of $150-200\ nm$ formed on the Mg samples. On the Zn samples no oxide layer was detected during the EBSD measurement, and no layer behaving like the oxide layer on the Mg could be observed in that case.

The production of the Zn samples can be considered successful, as the intended geometries were achieved and the experimental set-up was adhered to, also the orientation of the crystal was quite accurate. Potentially by using a better fitting gripper, such high bending stresses would not have formed and thus twinning could be observed in this experiment in the gauge part due to tensile stress, which was the actual intention for these experiments. Nevertheless, it could be proven that the tension twin, which theoretically should form due to the influence of the c/a ratio, was also formed, although the loading did not take place as planned. The measured misorientation and the pronounced flow plateaus also fit well together and the CRSS for the possible slip systems could be calculated.

To avoid twinning of the material while preparing the samples, it would be beneficial to perform EBSD-scans in between the preparation steps.

Furthermore, as the preparation in the FIB is very time-consuming, it is challenging to prevent the formation of the oxide layer on the Mg at all. It would be advantageous to test the samples as soon as they are finished. The next issue is that no correct EBSD measurements are possible

Conclusion

when a thicker oxide layer has formed, which in turn makes it difficult to determine the deformation mechanism after the experiments.

Due to the high compliance of the experimental setup and the resulting low apparent elastic modulus, a comparison is difficult. In addition, it can be expected that the oxide layer has also affected the elastic modulus, as the layer is pc and is expected to show a different behaviour. Although there were difficulties in the preparation of the samples and the implementation of the experiments, some results could be achieved that match literature data.

The comparison of the two materials is made difficult on the one hand by the high scatter and small number of samples, and on the other hand by the completely different behaviour, since Mg, for example, shows hardening and Zn shows pronounced flow plateaus. Nevertheless, the mechanical size effect can be shown for both samples, which is again a pleasing result.

If this experiment were to be repeated, it would be interesting to investigate other hexagonal materials because of their different c/a −ratios and to reduce the samples size to compare the deformation mechanisms in sub-micron sc tensile test specimens.

7. References

[1]   D. Kiener, J. Jeong, M. Alfreider, R. Konetschnik, and S. H. Oh, "Prospects of using small scale testing to examine different deformation mechanisms in nanoscale single crystals—a case study in MG," *Crystals*, vol. 11, no. 1, pp. 1–15, 2021.

[2]   J. R. Greer, W. C. Oliver, and W. D. Nix, "Size dependence of mechanical properties of gold at the micron scale in the absence of strain gradients," *Acta Mater.*, vol. 53, no. 6, pp. 1821–1830, 2005.

[3]   R. Dou and B. Derby, "A universal scaling law for the strength of metal micropillars and nanowires," *Scr. Mater.*, vol. 61, no. 5, pp. 524–527, 2009.

[4]   M. H. Yoo, "Slip, twinning, and fracture in hexagonal close-packed metals," *Metall. Trans. A*, vol. 12, no. 3, pp. 409–418, 1981.

[5]   G. Gottstein, *Materialwissenschaft und Werkstofftechnik*. 2015.

[6]   A. Jeklin, *Mineralogie*, no. July. 2016.

[7]   X. L. Nan, H. Y. Wang, Z. Q. Wu, E. S. Xue, L. Zhang, and Q. C. Jiang, "Effect of c/a axial ratio on Schmid factors in hexagonal close-packed metals," *Scr. Mater.*, vol. 68, no. 7, pp. 530–533, 2013.

[8]   X. L. Nan, H. Y. Wang, L. Zhang, J. B. Li, and Q. C. Jiang, "Calculation of Schmid factors in magnesium: Analysis of deformation behaviors," *Scr. Mater.*, vol. 67, no. 5, pp. 443–446, 2012.

[9]   G. Yang and S. J. Park, "Deformation of single crystals, polycrystalline materials, and thin films: A review," *Materials (Basel).*, vol. 12, no. 12, 2019.

[10]   E. Schmid and W. Boas, *Kristallplastizität*. 2021.

[11]   J. Zhang and S. P. Joshi, "Phenomenological crystal plasticity modeling and detailed micromechanical investigations of pure magnesium," *J. Mech. Phys. Solids*, vol. 60, no. 5, pp. 945–972, 2012.

[12]   C. HT, *Mechanical Behavior of Materials. 2. ed.* 2000.

References

[13] A. Luque, M. Ghazisaeidi, and W. A. Curtin, "Deformation modes in magnesium (0 0 0 1) and (011-1) single crystals: Simulations versus experiments," *Model. Simul. Mater. Sci. Eng.*, vol. 21, no. 4, pp. 1–15, 2013.

[14] E. Arzt, "SIZE EFFECTS IN MATERIALS DUE TO MICROSTRUCTURAL AND DIMENSIONAL CONSTRAINTS : A COMPARATIVE REVIEW," vol. 46, no. 16, pp. 5611–5626, 1998.

[15] T. A. Parthasarathy, S. I. Rao, D. M. Dimiduk, M. D. Uchic, and D. R. Trinkle, "Contribution to size effect of yield strength from the stochastics of dislocation source lengths in finite samples," vol. 56, pp. 313–316, 2007.

[16] R. W. Armstrong, "The influence of polycrystal grain size on several mechanical properties of materials," *Metall. Mater. Trans.*, vol. 1, no. 5, pp. 1169–1176, 1970.

[17] Q. Yu *et al.*, "Strong crystal size effect on deformation twinning," *Nature*, vol. 463, no. 7279, pp. 335–338, 2010.

[18] M. A. Meyers, O. Vöhringer, and V. A. Lubarda, "The onset of twinning in metals: A constitutive description," *Acta Mater.*, vol. 49, no. 19, pp. 4025–4039, 2001.

[19] J. W. Christian* and S. Mahajant, "DEFORMATION TWINNING," *Phys. Status Solidi*, vol. 191, no. 2, pp. 267–281, 1995.

[20] J. Jeong, M. Alfreider, R. Konetschnik, D. Kiener, and S. H. Oh, "In-situ TEM observation of {101¯2} twin-dominated deformation of Mg pillars: Twinning mechanism, size effects and rate dependency," *Acta Mater.*, vol. 158, pp. 407–421, 2018.

[21] J. R. Greer and J. T. M. De Hosson, "Plasticity in small-sized metallic systems: Intrinsic versus extrinsic size effect," *Prog. Mater. Sci.*, vol. 56, no. 6, pp. 654–724, 2011.

[22] J. R. Greer and W. D. Nix, "Nanoscale gold pillars strengthened through dislocation starvation," *Phys. Rev. B - Condens. Matter Mater. Phys.*, vol. 73, no. 24, pp. 1–6, 2006.

[23] D. M. Dimiduk, M. D. Uchic, and T. A. Parthasarathy, "Size-affected single-slip behavior of pure nickel microcrystals," *Acta Mater.*, vol. 53, no. 15, pp. 4065–4077, 2005.

[24] C. P. Frick, B. G. Clark, S. Orso, A. S. Schneider, and E. Arzt, "Size effect on strength and strain hardening of small-scale [1 1 1] nickel compression pillars," *Mater. Sci. Eng. A*, vol. 489, no. 1–2, pp. 319–329, 2008.

References

[25]   K. S. Ng and A. H. W. Ngan, "Effects of trapping dislocations within small crystals on their deformation behavior," *Acta Mater.*, vol. 57, no. 16, pp. 4902–4910, 2009.

[26]   B. Li and E. Ma, "Atomic shuffling dominated mechanism for deformation twinning in magnesium," *Phys. Rev. Lett.*, vol. 103, no. 3, pp. 1–4, 2009.

[27]   J. Wang, I. J. Beyerlein, J. P. Hirth, and C. N. Tomé, "Twinning dislocations on {1̄011} and {1̄013} planes in hexagonal close-packed crystals," *Acta Mater.*, vol. 59, no. 10, pp. 3990–4001, 2011.

[28]   J. N. Florando, M. Rhee, A. Arsenlis, M. M. Leblanc, and D. H. Lassila, "Calculation of the slip system activity in deformed zinc single crystals using digital 3-D image correlation data," *Philos. Mag. Lett.*, vol. 86, no. 12, pp. 795–805, 2006.

[29]   A. R. L. Bell and R. W. Cahn, "The dynamics of twinning and the interrelation of slip and twinning in zinc crystals," *Proc. R. Soc. London. Ser. A. Math. Phys. Sci.*, vol. 239, no. 1219, pp. 494–521, 1957.

[30]   J. Washburn and E. R. Parker, "Kinking in Zinc Single-Crystal Tension Specimens," *Jom*, vol. 4, no. 10, pp. 1076–1078, 1952.

[31]   M. J. Pfeifenberger *et al.*, "The use of femtosecond laser ablation as a novel tool for rapid micro-mechanical sample preparation," *Mater. Des.*, vol. 121, pp. 109–118, 2017.

[32]   D. Kiener and A. M. Minor, "Source-controlled yield and hardening of Cu(1 0 0) studied by in situ transmission electron microscopy," *Acta Mater.*, vol. 59, no. 4, pp. 1328–1337, 2011.

[33]   M. F. Horstemeyer, M. I. Baskes, and S. J. Plimpton, "Length scale and time scale effects on the plastic flow of fcc metals," *Acta Mater.*, vol. 49, no. 20, pp. 4363–4374, 2001.

[34]   O. Torrents Abad, J. M. Wheeler, J. Michler, A. S. Schneider, and E. Arzt, "Temperature-dependent size effects on the strength of Ta and W micropillars," *Acta Mater.*, vol. 103, pp. 483–494, 2016.

8. List of figures

List of figures